Online Supplement to "Prediction of bubbles in presence of α-stable aggregates moving averages"

Gilles de Truchis, Sébastien Fries, Arthur Thomas

This Online Supplement accompanies the main paper by providing comprehensive Monte Carlo results and detailed application diagnostics.

Sections S.1 and S.2 present the complete Monte Carlo study that supports the summary in Section 4 of the main text. Section S.3 provides the full empirical analysis of the OVX index summarized in Section 5.

The supplement is organized as follows.

Sections S.1 and S.2: Monte Carlo Study and subsampling. This section documents the finite-sample performance of the minimum distance estimator. Section S.1 reports the estimation accuracy results across three distributional settings (Cauchy, symmetric α-stable, and general α-stable). Section S.2 presents the subsampling methodology used to verify asymptotic normality. Section S.2.2 reports results in the original parameter space $\theta = (\psi_1, \psi_2, \varsigma_1, \varsigma_2, \alpha)$, documenting the identification difficulties of the individual scale parameters. Section S.2.3 presents results in the reparameterized space $\vartheta = (\psi_1, \psi_2, \sigma, \pi_1, \alpha)$. Section S.2.4 reports the criterion difference test for $H_0 : \pi_1 = 1/2$. Section S.2.5 reports restricted subsampling diagnostics under $\pi_1 = 1/2$. Section S.2.6 repeats the analysis under the true constraint $\pi_1 = 0.4375$, isolating finite-sample convergence from specification bias.

Section S.3: Application to the OVX Index.. This section provides the complete empirical analysis of the CBOE Crude Oil ETF Volatility Index. Section S.3.1 reports estimation results under three distributional specifications. Section S.3.2 presents the deconvolution into latent components. Section S.3.3 develops the in-sample forecasting exercise for the 2020 oil market disruption, including the pattern-matching algorithm, crash probability computations, and risk threshold analysis. Section S.3.4 collects per-component graphical diagnostics.

S.1. Monte Carlo estimation accuracy

This subsection reports the full Monte Carlo estimation accuracy results that are summarized in Section 4.1 of the main paper. The observed process is generated by the aggregation of two independent α-stable AR(1) processes as specified in equations (4.1)–(4.2) of the main text. Table S.1 reports the bias, root mean square error (RMSE), and mean relative error (MRE) across all scenarios and sample sizes.

Table S.1: Monte Carlo estimation accuracy for α-stable AR(1) aggregates (1,000 replications)

		$T = 250$			$T = 500$			$T = 1000$		
θ	True	Bias	RMSE	MRE	Bias	RMSE	MRE	Bias	RMSE	MRE
Panel A: Cauchy ($\mathcal{S}1\mathcal{S}$, $\alpha = 1$, $\beta = 0$)										
ψ_1	0.800	−0.008	0.050	0.046	−0.004	0.030	0.029	−0.002	0.020	0.019
ς_1	0.700	−0.023	0.322	0.368	0.002	0.249	0.275	−0.002	0.179	0.196
ψ_2	0.300	−0.035	0.169	0.455	−0.025	0.128	0.333	−0.012	0.089	0.223
ς_2	0.900	−0.035	0.279	0.249	−0.015	0.193	0.171	−0.007	0.134	0.119
Panel B: Symmetric α-stable ($\mathcal{S}\alpha\mathcal{S}$, $\alpha = 1.5$, $\beta = 0$)										
ψ_1	0.800	0.013	0.081	0.073	0.000	0.062	0.057	−0.005	0.046	0.044
ς_1	0.700	−0.101	0.276	0.325	−0.021	0.216	0.247	0.019	0.168	0.195
ψ_2	0.300	−0.127	0.209	0.600	−0.096	0.190	0.529	−0.072	0.148	0.391
ς_2	0.900	−0.124	0.235	0.212	−0.098	0.197	0.175	−0.071	0.153	0.135
α	1.500	−0.037	0.173	0.086	−0.014	0.127	0.065	−0.004	0.088	0.046
Panel C: General α-stable ($\mathcal{G}\alpha\mathcal{S}$, $\alpha = 1.5$, $\beta = 0.3$)										
ψ_1	0.800	−0.005	0.091	0.084	−0.015	0.073	0.069	−0.013	0.057	0.055
ς_1	0.700	−0.054	0.285	0.335	0.013	0.234	0.278	0.026	0.200	0.236
ψ_2	0.300	−0.089	0.208	0.594	−0.068	0.186	0.510	−0.052	0.146	0.388
ς_2	0.900	−0.124	0.234	0.211	−0.115	0.205	0.179	−0.092	0.178	0.154
α	1.500	−0.026	0.164	0.083	−0.009	0.120	0.060	−0.003	0.082	0.042
β	0.300	−0.007	0.262	0.628	−0.003	0.186	0.457	−0.001	0.132	0.328

Notes: True parameter values are $\psi_1 = 0.8$, $\psi_2 = 0.3$, $\varsigma_1 = 0.7$, $\varsigma_2 = 0.9$. MRE denotes the mean relative error $\mathbb{E}[|\hat{\theta} - \theta_0|/|\theta_0|]$. Estimation uses the empirical characteristic function with uniform weights on a 10×10 grid in $[-0.5, 0.5]^2$.

Several patterns emerge from Table S.1. First, the dominant autoregressive coefficient ψ_1 is precisely estimated across all settings, with MRE below 5% in the $\mathcal{S}1\mathcal{S}$ case and below 9% even in the $\mathcal{G}\alpha\mathcal{S}$ case for $T = 250$. Second, the smaller coefficient ψ_2 and the combined scale parameters ς_1, ς_2 exhibit substantially higher relative errors, reflecting the inherent difficulty in disentangling the individual component contributions from the aggregate signal. Third, the tail index α is recovered with high accuracy (MRE around 8% at $T = 250$, declining to 4–5% at $T = 1{,}000$), confirming the informational content of the empirical characteristic function for identifying heavy-tail behavior. Fourth, in the $\mathcal{G}\alpha\mathcal{S}$ setting, the asymmetry parameter β is the most difficult to estimate (MRE of 63% at $T = 250$), although its identification is not required for the autoregressive and scale parameters. Across all scenarios, the RMSE and MRE decrease consistently with T, confirming the good finite-sample behavior of the estimator.

S.2. Subsampling Diagnostics and Convergence Analysis

S.2.1. Subsampling methodology

This section describes the subsampling procedure used to assess the finite-sample convergence of our minimum distance estimator toward the limiting normal distribution predicted by Proposition 2.1 of the

main paper. The methodology follows Politis and Romano (1994) and Politis et al. (1999) and provides a nonparametric way to evaluate the sampling distribution of $\sqrt{n}(\hat{\theta}_n - \theta_0)$ without requiring explicit knowledge of the asymptotic variance matrix $\Sigma^{-1}\Omega\Sigma^{-1}$.

Given a full sample of size n, we construct non-overlapping subsamples of size $b < n$:

$$\mathcal{X}_b^{(i)} = \{\mathcal{X}_{(i-1)b+1}, \ldots, \mathcal{X}_{ib}\}, \quad i = 1, \ldots, N_b = \lfloor n/b \rfloor. \tag{S.1}$$

Following Politis et al. (1999), we set $b = \lfloor n^{2/3} \rfloor$, which ensures that $b \to \infty$, $b/n \to 0$, and satisfies the higher-order requirements for the subsampling approximation to be valid under weak dependence.

Since the individual scale parameters ς_1 and ς_2 exhibit poor finite-sample convergence in the original parameterization (see Section S.2.2 below), we apply a post-estimation reparameterization:

$$\vartheta = (\rho_1, \rho_2, \sigma, \pi_1, \alpha), \quad \text{where} \quad \sigma = \varsigma_1 + \varsigma_2, \quad \pi_1 = \frac{\varsigma_1}{\sigma}. \tag{S.2}$$

The scaled subsample deviations are then constructed as

$$Z_b^{(i)} = \sqrt{b}\left(\hat{\vartheta}_b^{(i)} - \hat{\vartheta}_n\right), \quad i = 1, \ldots, N_b, \tag{S.3}$$

where $\hat{\vartheta}_n$ is the full-sample MDE estimator mapped to the reparameterized space. Under the conditions of Proposition 2.1, and following the theoretical framework of Politis and Romano (1994), these scaled deviations should approximately follow the same asymptotic distribution as $\sqrt{n}(\hat{\vartheta}_n - \vartheta_0)$.

For each Monte Carlo replication $m = 1, \ldots, M$ and a given sample size n, we proceed as follows:

(ι) Generate a time series $\mathcal{X}_t$ from the true model with parameters θ_0.

($\iota\iota$) Compute the full-sample MDE estimator $\hat{\theta}_n$ and map it to the reparameterized space $\hat{\vartheta}_n$.

($\iota\iota\iota$) Extract $N_b = \lfloor n/b \rfloor$ non-overlapping subsamples with $b = \lfloor n^{2/3} \rfloor$.

($\iota\nu$) For each subsample $i = 1, \ldots, N_b$, compute the subsample estimator $\hat{\vartheta}_b^{(i)}$.

(ν) Construct the scaled deviations $Z_b^{(i)}$ according to (S.3).

The pooled non-overlapping block deviations across all Monte Carlo replications are subjected to several normality diagnostics for each parameter component. First, we compute summary statistics including the sample mean, standard deviation, skewness, and excess kurtosis. Second, we report the Shapiro-Wilk (SW) and Jarque-Bera (JB) rejection rates at the 5% significance level. Third, we assess confidence interval coverage using both quantile-based and normal-approximation intervals at the 90% and 95% levels; for this purpose, confidence intervals are constructed from thinned overlapping blocks (using all $n - b + 1$ overlapping subsamples with appropriate thinning to reduce dependence), while normality diagnostics use the non-overlapping blocks to avoid dependence contamination.

Table S.3 summarizes the key subsampling results for the unrestricted estimator in the reparameterized space, reporting results for $n \in \{1{,}000, 10{,}000, 100{,}000\}$.

Table S.4 reports the restricted subsampling results under the true constraint $\pi_1 = 0.4375$ for the same sample sizes.

Table S.2: Monte Carlo Design Parameters

Sample Size n	Subsample Size b	Non-overlapping Blocks N_b	MC Replications M
250	39	6	200
500	62	8	200
1,000	99	10	200
10,000	464	21	200
50,000	1,357	36	200
100,000	2,154	46	200

Notes: The subsample size is set to $b = \lfloor n^{2/3} \rfloor$ following Politis et al. (1999). $N_b = \lfloor n/b \rfloor$ denotes the number of non-overlapping blocks per replication.

Table S.3: Summary of unrestricted subsampling results (reparameterized space)

							Quantile CI		Normal CI		
n	Param.	True	Avg. Est.	Std. Est.	Dev. Mean	Skew	Kurt	qCov90	qCov95	nCov90	nCov95
	ψ_1	0.80	0.812	0.086	−0.15	−0.41	−0.62	0.555	0.605	0.690	0.745
	ψ_2	0.30	0.296	0.157	0.57	0.06	−0.96	0.450	0.455	0.595	0.660
1,000	σ	1.60	1.543	0.188	−0.55	0.19	−0.52	0.600	0.635	0.665	0.715
	π_1	0.4375	0.414	0.162	−0.47	−0.23	−0.42	0.285	0.315	0.510	0.610
	α	1.50	1.493	0.093	0.13	−0.15	−0.59	0.800	0.815	0.825	0.885
	ψ_1	0.80	0.786	0.029	0.43	0.18	−0.70	0.530	0.620	0.770	0.885
	ψ_2	0.30	0.260	0.055	1.15	0.09	−0.97	0.505	0.520	0.705	0.825
10,000	σ	1.60	1.599	0.053	−1.38	0.01	−0.69	0.825	0.885	0.885	0.955
	π_1	0.4375	0.473	0.058	−1.55	−0.72	−0.44	0.210	0.230	0.490	0.735
	α	1.50	1.498	0.028	0.00	−0.02	−0.35	0.895	0.925	0.900	0.940
	ψ_1	0.80	0.778	0.013	1.11	0.89	0.85	0.145	0.155	0.155	0.170
	ψ_2	0.30	0.249	0.025	1.75	−0.38	−0.02	0.175	0.200	0.170	0.205
100,000	σ	1.60	1.609	0.017	−1.48	−0.31	−0.12	0.795	0.850	0.905	0.950
	π_1	0.4375	0.491	0.028	−2.59	−1.25	1.43	0.145	0.155	0.145	0.145
	α	1.50	1.501	0.009	−0.05	−0.00	−0.20	0.910	0.960	0.925	0.965

Notes: Avg. Est. and Std. Est. are computed over $M = 200$ replications. Dev. Mean, Skew, and Kurt refer to the mean, skewness, and excess kurtosis of the non-overlapping block scaled deviations $Z_b^{(i)}$. qCov and nCov denote the average coverage of quantile-based and normal-approximation confidence intervals. Complete results for all sample sizes are in Tables S.3–S.8.

S.2.2. Unrestricted subsampling in the original parameterization

This subsection reports the full subsampling diagnostics when estimation is performed in the original parameter space $\theta = (\rho_1, \rho_2, \varsigma_1, \varsigma_2, \alpha)$, without the reparameterization (σ, π_1) and without any restriction. Tables S.5–S.10 display the scaled subsample deviation statistics, normality test rejection rates, and confidence interval coverage for each sample size. Figures S.1–S.6 provide the corresponding graphical diagnostics. For each parameter and sample size, histograms, Q-Q plots, and kernel density estimates of the standardized non-overlapping block deviations are displayed.

S.2.3. Unrestricted subsampling in the reparameterized space

We now report the subsampling diagnostics in the reparameterized space $\vartheta = (\rho_1, \rho_2, \sigma, \pi_1, \alpha)$, where $\sigma = \varsigma_1 + \varsigma_2$ and $\pi_1 = \varsigma_1/\sigma$. Estimation is performed in the original $(\varsigma_1, \varsigma_2)$ space; the transformation is applied

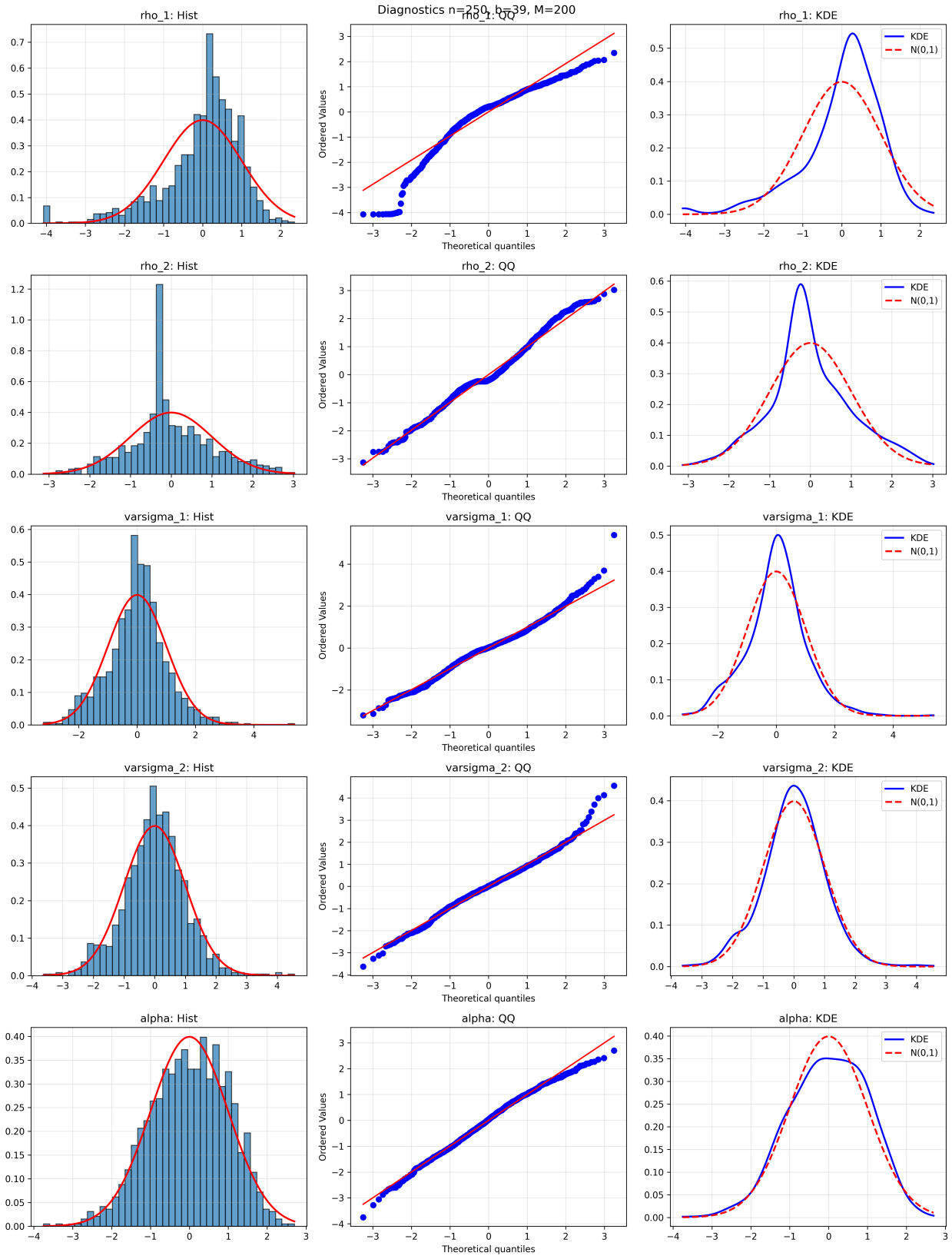

Figure S.1: Diagnostic plots for scaled subsample deviations (original parameterization) at $n = 250$. For each parameter (rows): histogram with standard normal overlay (left), Q-Q plot (center), and kernel density estimate vs. $\mathcal{N}(0, 1)$ (right).

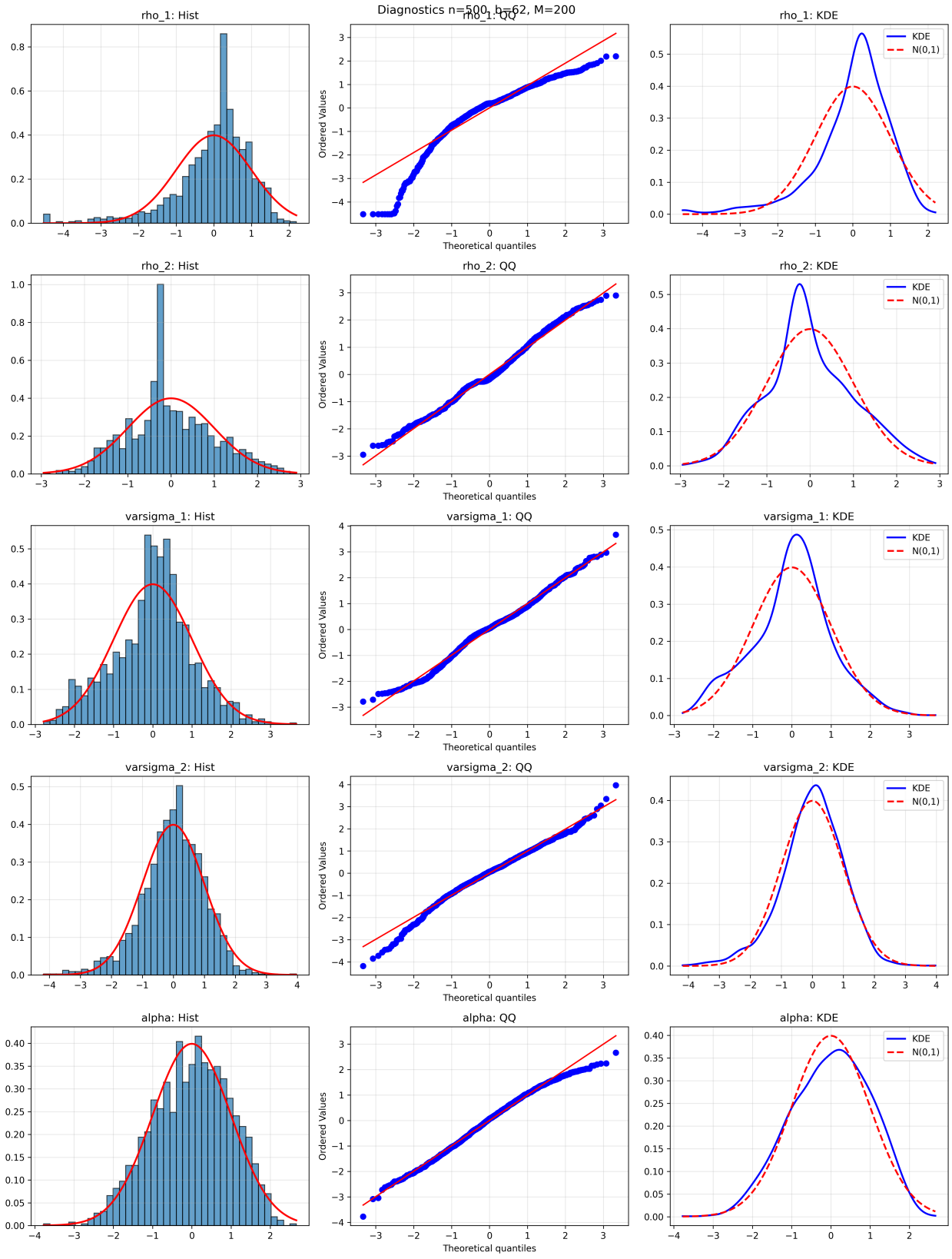

Figure S.2: Diagnostic plots for scaled subsample deviations (original parameterization) at $n = 500$. See caption to Figure S.1 for details.

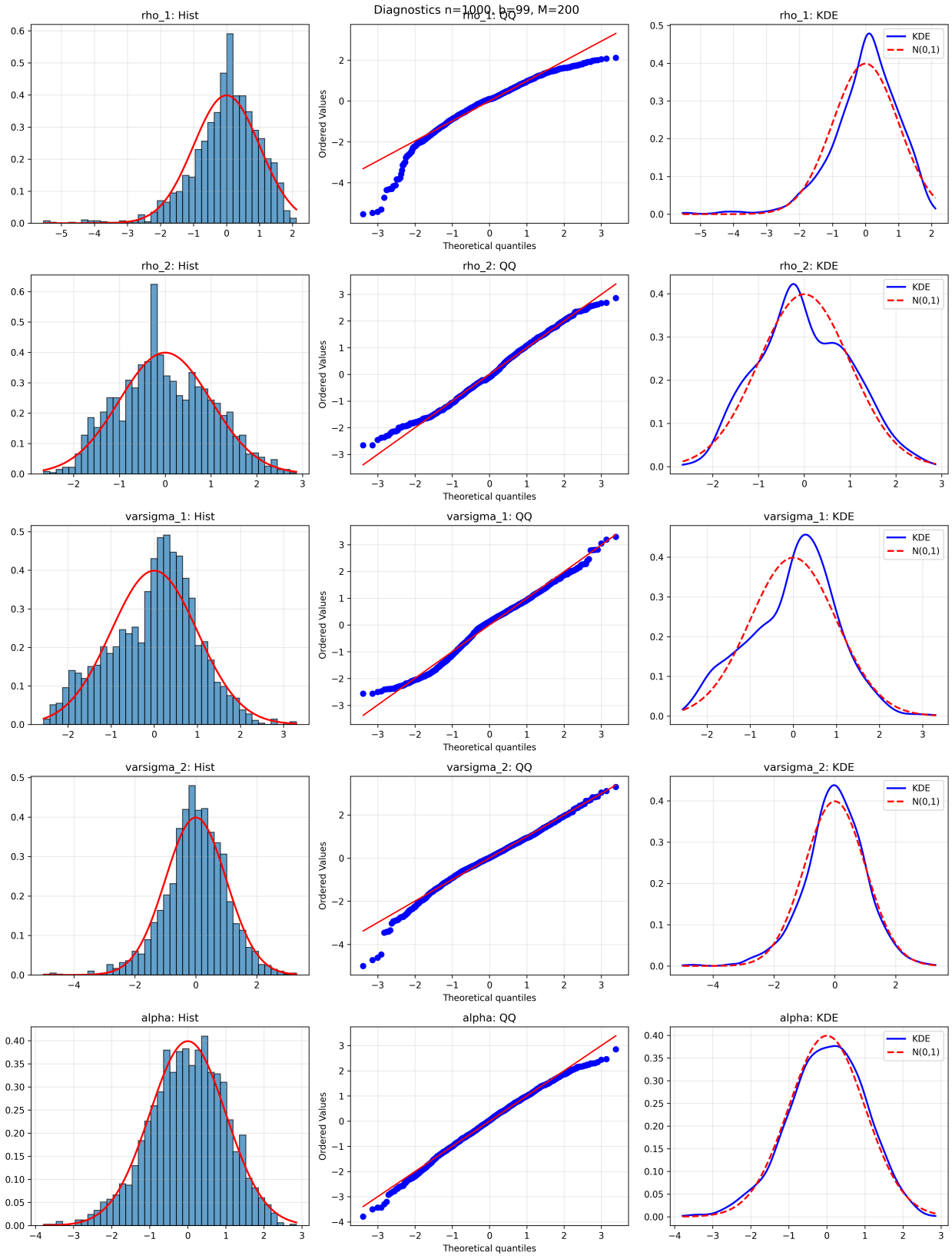

Figure S.3: Diagnostic plots for scaled subsample deviations (original parameterization) at $n = 1,000$. See caption to Figure S.1 for details.

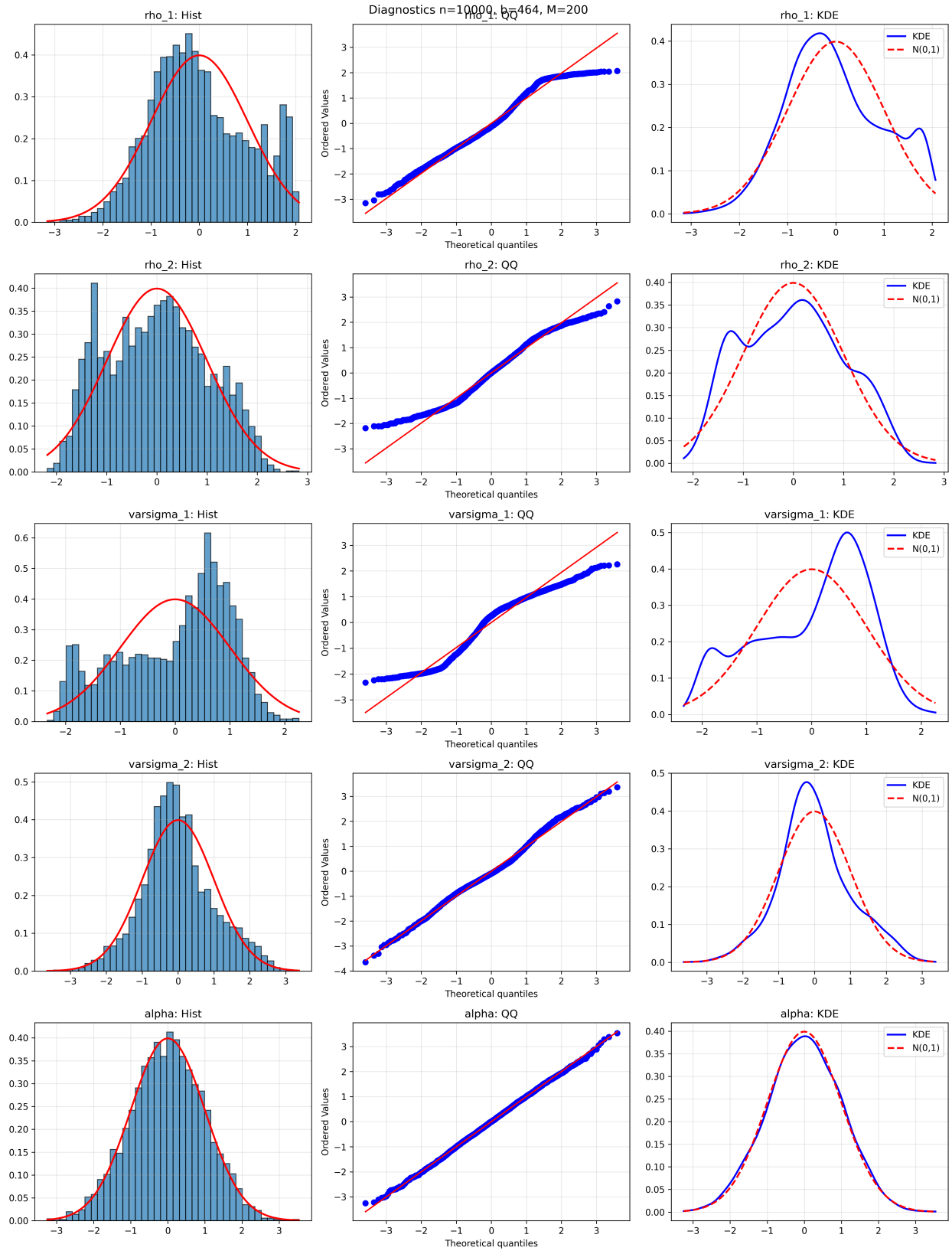

Figure S.4: Diagnostic plots for scaled subsample deviations (original parameterization) at $n = 10,000$. See caption to Figure S.1 for details.

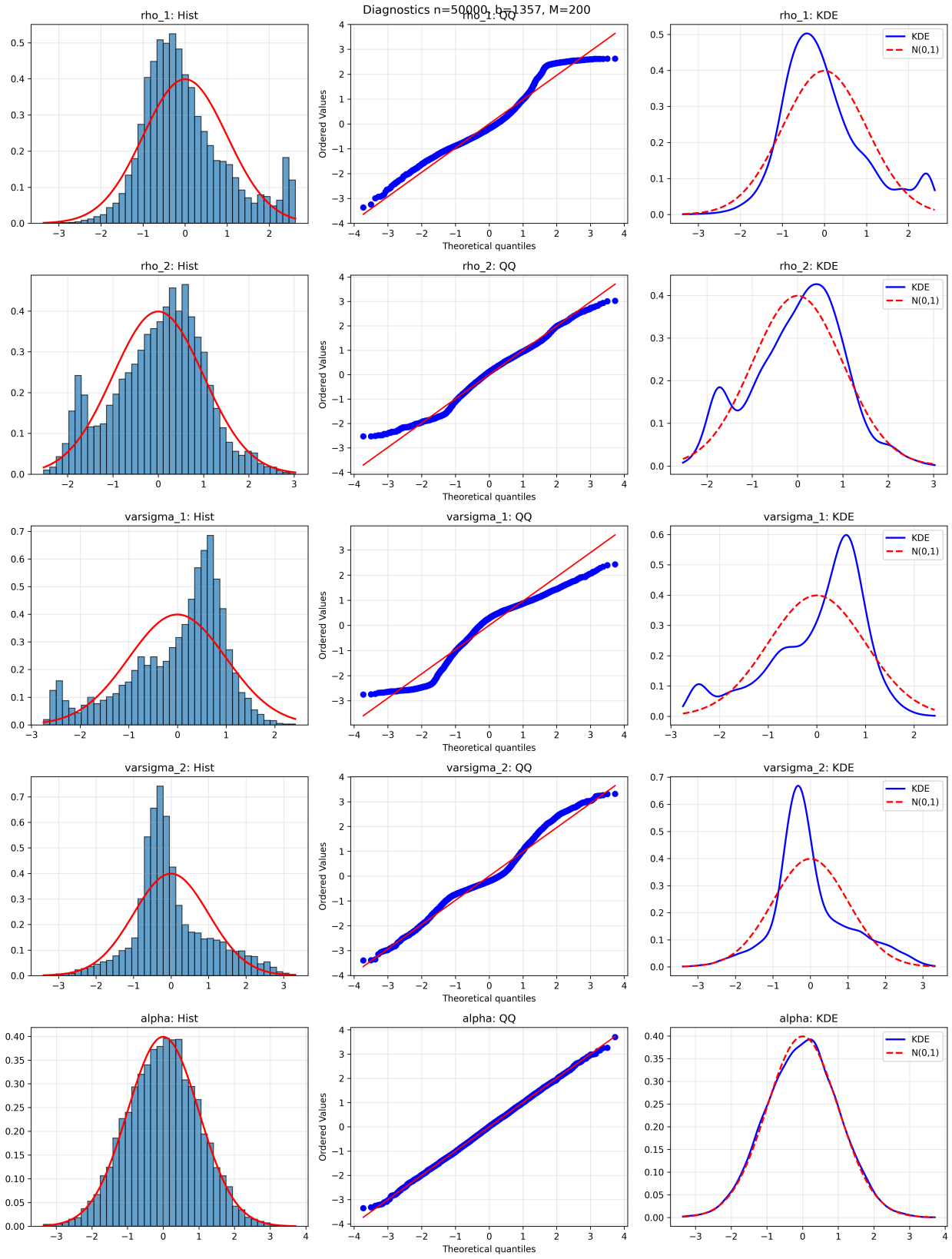

Figure S.5: Diagnostic plots for scaled subsample deviations (original parameterization) at $n = 50,000$. See caption to Figure S.1 for details. .

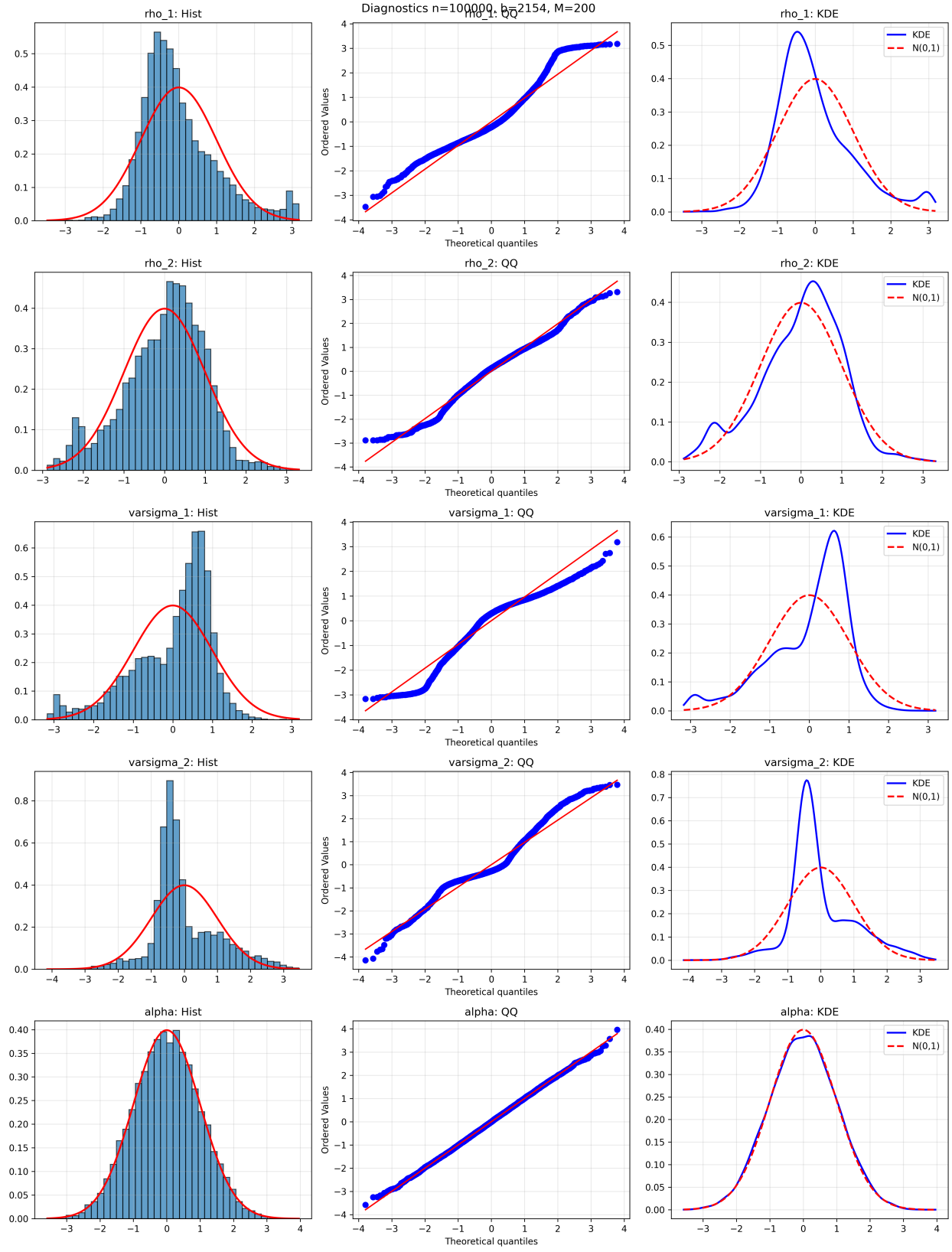

Figure S.6: Diagnostic plots for scaled subsample deviations (original parameterization) at $n = 100,000$. See caption to Figure S.1 for details.

Table S.4: Summary of restricted subsampling results under $\pi_1 = 0.4375$ (true value)

							Quantile CI		Normal CI		
n	Param.	True	Avg. Est.	Std. Est.	Dev. Mean	Skew	Kurt	qCov90	qCov95	nCov90	nCov95
1,000	ψ_1	0.80	0.761	0.131	−0.51	−0.49	−0.34	0.750	0.780	0.860	0.885
	ψ_2	0.30	0.321	0.190	0.42	0.05	−1.07	0.370	0.375	0.510	0.595
	σ	1.60	1.594	0.151	0.12	0.09	−0.47	0.680	0.740	0.750	0.810
	α	1.50	1.496	0.090	0.22	−0.11	−0.61	0.800	0.820	0.825	0.880
10,000	ψ_1	0.80	0.799	0.010	−0.60	−0.70	0.19	0.890	0.920	0.965	0.980
	ψ_2	0.30	0.298	0.050	0.37	0.13	−1.04	0.775	0.775	0.865	0.920
	σ	1.60	1.599	0.044	0.09	0.14	−0.44	0.830	0.880	0.860	0.925
	α	1.50	1.498	0.028	0.12	0.01	−0.36	0.880	0.915	0.895	0.925
100,000	ψ_1	0.80	0.800	0.003	−0.25	−0.77	1.43	0.920	0.955	0.950	0.980
	ψ_2	0.30	0.301	0.017	0.04	−0.01	−0.11	0.925	0.975	0.900	0.980
	σ	1.60	1.601	0.014	0.02	0.07	−0.21	0.885	0.935	0.895	0.945
	α	1.50	1.500	0.008	0.06	0.01	−0.19	0.920	0.960	0.940	0.965

Notes: See notes to Table S.3. Estimation under the true restriction $\pi_1 = \varsigma_1/\sigma = 0.4375$. Complete results for all sample sizes are in Tables S.9–S.14.

Table S.5: Subsampling results (original parameterization) for $n = 250$ ($b = 39$, $N_b = 6$, $M = 200$)

									Quantile CI		Normal CI		
Parameter	True	Avg Est.	Std Est.	Dev. Mean	Dev. Std	Skew	Kurt	SW Rej.	JB Rej.	qCov90	qCov95	nCov90	nCov95
ρ_1	0.800	0.782	0.128	−0.309	1.327	−0.518	−0.748	0.175	0.000	0.620	0.630	0.720	0.790
ρ_2	0.300	0.304	0.240	0.390	1.493	0.190	−0.931	0.230	0.000	0.270	0.290	0.355	0.435
ς_1	0.700	0.696	0.385	−0.103	2.466	0.097	−0.787	0.180	0.000	0.280	0.310	0.420	0.485
ς_2	0.900	0.830	0.209	−0.042	1.928	−0.067	−0.751	0.055	0.000	0.600	0.665	0.590	0.685
α	1.500	1.483	0.162	0.253	2.067	−0.107	−0.920	0.065	0.000	0.650	0.690	0.795	0.870

Notes: All results are in the original parameter space $(\rho_1, \rho_2, \varsigma_1, \varsigma_2, \alpha)$ without reparameterization or restriction. SW and JB rejection rates are at the 5% level. qCov and nCov denote quantile-based and normal-approximation CI coverage. Confidence intervals are constructed from thinned overlapping blocks; normality diagnostics use non-overlapping blocks.

post-estimation. We compute scaled subsample deviations $\sqrt{b}(\hat{\vartheta}_b^{(i)} - \hat{\vartheta}_n)$ using non-overlapping blocks of size $b = \lfloor n^{2/3} \rfloor$. For each sample size $n \in \{250, 500, 1,000, 10,000, 50,000, 100,000\}$, we generate $M = 200$ Monte Carlo replications and compute $N_b = \lfloor n/b \rfloor$ non-overlapping blocks per replication. Confidence interval coverage is assessed using all $n - b + 1$ overlapping blocks per replication. The descriptive statistics in Tables S.11–S.16 report the mean, standard deviation, skewness, and excess kurtosis of the non-overlapping block deviations, alongside the Shapiro-Wilk (SW) and Jarque-Bera (JB) rejection rates at the 5% significance level, and the average coverage of 90% and 95% confidence intervals (both quantile-based and normal-approximation).

Table S.6: Subsampling results (original parameterization) for $n = 500$ ($b = 62$, $N_b = 8$, $M = 200$)

									Quantile CI		Normal CI		
Parameter	True	Avg Est.	Std Est.	Dev. Mean	Dev. Std	Skew	Kurt	SW Rej.	JB Rej.	qCov90	qCov95	nCov90	nCov95
ρ_1	0.800	0.804	0.111	−0.312	1.499	−0.565	−0.433	0.295	0.045	0.585	0.630	0.635	0.750
ρ_2	0.300	0.297	0.198	0.528	1.960	0.151	−0.762	0.315	0.020	0.395	0.400	0.525	0.575
ς_1	0.700	0.673	0.354	−0.303	2.988	0.111	−0.747	0.235	0.035	0.280	0.285	0.440	0.550
ς_2	0.900	0.849	0.194	−0.030	2.185	−0.144	−0.646	0.080	0.000	0.475	0.545	0.475	0.600
α	1.500	1.489	0.113	0.209	2.404	−0.169	−0.780	0.075	0.000	0.765	0.810	0.855	0.915

Notes: See notes to Table S.5.

Table S.7: Subsampling results (original parameterization) for $n = 1,000$ ($b = 99$, $N_b = 10$, $M = 200$)

									Quantile CI		Normal CI		
Parameter	True	Avg Est.	Std Est.	Dev. Mean	Dev. Std	Skew	Kurt	SW Rej.	JB Rej.	qCov90	qCov95	nCov90	nCov95
ρ_1	0.800	0.812	0.086	−0.152	1.564	−0.415	−0.616	0.260	0.015	0.565	0.605	0.680	0.755
ρ_2	0.300	0.296	0.157	0.573	2.530	0.062	−0.963	0.300	0.010	0.445	0.465	0.600	0.655
ς_1	0.700	0.662	0.301	−0.641	3.757	−0.002	−0.836	0.265	0.020	0.330	0.335	0.445	0.535
ς_2	0.900	0.881	0.163	0.096	2.391	−0.055	−0.382	0.045	0.005	0.420	0.545	0.480	0.585
α	1.500	1.493	0.093	0.128	2.493	−0.153	−0.586	0.045	0.010	0.795	0.815	0.825	0.890

Notes: See notes to Table S.5.

Table S.8: Subsampling results (original parameterization) for $n = 10,000$ ($b = 464$, $N_b = 21$, $M = 200$)

									Quantile CI		Normal CI		
Parameter	True	Avg Est.	Std Est.	Dev. Mean	Dev. Std	Skew	Kurt	SW Rej.	JB Rej.	qCov90	qCov95	nCov90	nCov95
ρ_1	0.800	0.786	0.029	0.427	2.386	0.177	−0.700	0.255	0.010	0.530	0.650	0.770	0.890
ρ_2	0.300	0.260	0.055	1.148	4.591	0.089	−0.973	0.265	0.000	0.505	0.520	0.710	0.825
ς_1	0.700	0.758	0.109	−2.362	7.256	−0.433	−0.892	0.485	0.010	0.290	0.360	0.555	0.750
ς_2	0.900	0.841	0.075	0.984	3.812	0.208	−0.141	0.170	0.035	0.155	0.180	0.160	0.240
α	1.500	1.498	0.028	0.003	2.781	−0.025	−0.355	0.045	0.025	0.890	0.925	0.900	0.930

Notes: See notes to Table S.5.

Table S.9: Subsampling results (original parameterization) for $n = 50,000$ ($b = 1,357$, $N_b = 36$, $M = 200$)

									Quantile CI		Normal CI		
Parameter	True	Avg Est.	Std Est.	Dev. Mean	Dev. Std	Skew	Kurt	SW Rej.	JB Rej.	qCov90	qCov95	nCov90	nCov95
ρ_1	0.800	0.779	0.016	0.882	2.849	0.708	0.292	0.595	0.265	0.185	0.210	0.290	0.450
ρ_2	0.300	0.250	0.031	1.378	5.453	−0.192	−0.421	0.255	0.000	0.270	0.285	0.285	0.400
ς_1	0.700	0.782	0.065	−3.581	9.370	−0.828	0.112	0.820	0.285	0.170	0.175	0.170	0.245
ς_2	0.900	0.824	0.047	2.041	5.382	0.540	0.440	0.610	0.250	0.150	0.160	0.150	0.170
α	1.500	1.501	0.014	−0.035	2.805	−0.005	−0.244	0.055	0.025	0.870	0.915	0.850	0.920

Notes: See notes to Table S.5.

Table S.10: Subsampling results (original parameterization) for $n = 100{,}000$ ($b = 2{,}154$, $N_b = 46$, $M = 200$)

									Quantile CI		Normal CI		
Parameter	True	Avg Est.	Std Est.	Dev. Mean	Dev. Std	Skew	Kurt	SW Rej.	JB Rej.	qCov90	qCov95	nCov90	nCov95
ρ_1	0.800	0.778	0.013	1.104	2.944	0.889	0.849	0.770	0.635	0.155	0.155	0.145	0.175
ρ_2	0.300	0.249	0.025	1.750	5.651	−0.382	−0.019	0.360	0.050	0.175	0.210	0.170	0.200
ς_1	0.700	0.790	0.050	−4.298	10.040	−0.925	0.467	0.895	0.610	0.145	0.150	0.140	0.145
ς_2	0.900	0.819	0.040	2.816	5.924	0.666	0.639	0.860	0.460	0.140	0.145	0.135	0.140
α	1.500	1.501	0.009	−0.051	2.867	−0.004	−0.196	0.060	0.040	0.930	0.960	0.930	0.965

Notes: See notes to Table S.5.

Table S.11: Subsampling results (reparameterized) for $n = 250$ ($b = 39$, $N_b = 6$, $M = 200$)

									Quantile CI		Normal CI		
Parameter	True	Avg Est.	Std Est.	Dev. Mean	Dev. Std	Skew	Kurt	SW Rej.	JB Rej.	qCov90	qCov95	nCov90	nCov95
ρ_1	0.800	0.782	0.128	−0.309	1.327	−0.518	−0.748	0.175	0.000	0.620	0.630	0.720	0.800
ρ_2	0.300	0.304	0.240	0.390	1.493	0.190	−0.931	0.230	0.000	0.270	0.290	0.350	0.430
σ	1.600	1.527	0.303	−0.146	3.038	0.134	−0.851	0.075	0.000	0.510	0.550	0.590	0.695
π_1	0.438	0.430	0.199	−0.092	1.258	0.044	−0.464	0.305	0.000	0.330	0.370	0.465	0.535
α	1.500	1.483	0.162	0.253	2.067	−0.107	−0.920	0.065	0.000	0.650	0.685	0.800	0.870

Notes: All results are in the reparameterized space $(\rho_1, \rho_2, \sigma, \pi_1, \alpha)$. SW and JB rejection rates are at the 5% level. qCov and nCov denote quantile-based and normal-approximation CI coverage. Confidence intervals are constructed from thinned overlapping blocks; normality diagnostics use non-overlapping blocks.

Table S.12: Subsampling results (reparameterized) for $n = 500$ ($b = 62$, $N_b = 8$, $M = 200$)

									Quantile CI		Normal CI		
Parameter	True	Avg Est.	Std Est.	Dev. Mean	Dev. Std	Skew	Kurt	SW Rej.	JB Rej.	qCov90	qCov95	nCov90	nCov95
ρ_1	0.800	0.804	0.111	−0.312	1.499	−0.565	−0.433	0.295	0.045	0.580	0.630	0.635	0.755
ρ_2	0.300	0.297	0.198	0.528	1.960	0.151	−0.762	0.315	0.020	0.385	0.400	0.525	0.575
σ	1.600	1.522	0.231	−0.333	3.273	0.220	−0.678	0.075	0.005	0.565	0.595	0.615	0.685
π_1	0.438	0.420	0.195	−0.201	1.621	−0.036	−0.238	0.375	0.080	0.300	0.320	0.500	0.575
α	1.500	1.489	0.113	0.209	2.404	−0.169	−0.780	0.075	0.000	0.765	0.800	0.855	0.915

Notes: See notes to Table S.11.

Table S.13: Subsampling results (reparameterized) for $n = 1,000$ ($b = 99$, $N_b = 10$, $M = 200$)

									Quantile CI		Normal CI		
Parameter	True	Avg Est.	Std Est.	Dev. Mean	Dev. Std	Skew	Kurt	SW Rej.	JB Rej.	qCov90	qCov95	nCov90	nCov95
ρ_1	0.800	0.812	0.086	−0.152	1.564	−0.415	−0.616	0.260	0.015	0.555	0.605	0.690	0.745
ρ_2	0.300	0.296	0.157	0.573	2.530	0.062	−0.963	0.300	0.010	0.450	0.455	0.595	0.660
σ	1.600	1.543	0.188	−0.545	3.759	0.190	−0.525	0.105	0.025	0.600	0.635	0.665	0.715
π_1	0.438	0.414	0.162	−0.467	2.010	−0.228	−0.420	0.380	0.070	0.285	0.315	0.510	0.610
α	1.500	1.493	0.093	0.128	2.493	−0.153	−0.586	0.045	0.010	0.800	0.815	0.825	0.885

Notes: See notes to Table S.11.

Table S.14: Subsampling results (reparameterized) for $n = 10,000$ ($b = 464$, $N_b = 21$, $M = 200$)

									Quantile CI		Normal CI		
Parameter	True	Avg Est.	Std Est.	Dev. Mean	Dev. Std	Skew	Kurt	SW Rej.	JB Rej.	qCov90	qCov95	nCov90	nCov95
ρ_1	0.800	0.786	0.029	0.427	2.386	0.177	−0.700	0.255	0.010	0.530	0.620	0.770	0.885
ρ_2	0.300	0.260	0.055	1.148	4.591	0.089	−0.973	0.265	0.000	0.505	0.520	0.705	0.825
σ	1.600	1.599	0.053	−1.377	5.329	0.008	−0.692	0.085	0.005	0.825	0.885	0.885	0.955
π_1	0.438	0.473	0.058	−1.554	3.897	−0.724	−0.437	0.735	0.070	0.210	0.230	0.490	0.735
α	1.500	1.498	0.028	0.003	2.781	−0.025	−0.355	0.045	0.025	0.895	0.925	0.900	0.940

Notes: See notes to Table S.11.

Table S.15: Subsampling results (reparameterized) for $n = 50,000$ ($b = 1,357$, $N_b = 36$, $M = 200$)

									Quantile CI		Normal CI		
Parameter	True	Avg Est.	Std Est.	Dev. Mean	Dev. Std	Skew	Kurt	SW Rej.	JB Rej.	qCov90	qCov95	nCov90	nCov95
ρ_1	0.800	0.779	0.016	0.882	2.849	0.708	0.292	0.595	0.265	0.190	0.205	0.305	0.450
ρ_2	0.300	0.250	0.031	1.378	5.453	−0.192	−0.421	0.255	0.000	0.270	0.280	0.305	0.415
σ	1.600	1.606	0.026	−1.540	5.833	−0.201	−0.429	0.030	0.005	0.825	0.875	0.900	0.940
π_1	0.438	0.487	0.035	−2.185	5.131	−1.158	0.980	0.965	0.720	0.175	0.180	0.155	0.190
α	1.500	1.501	0.014	−0.035	2.805	−0.005	−0.244	0.055	0.025	0.850	0.905	0.845	0.915

Notes: See notes to Table S.11.

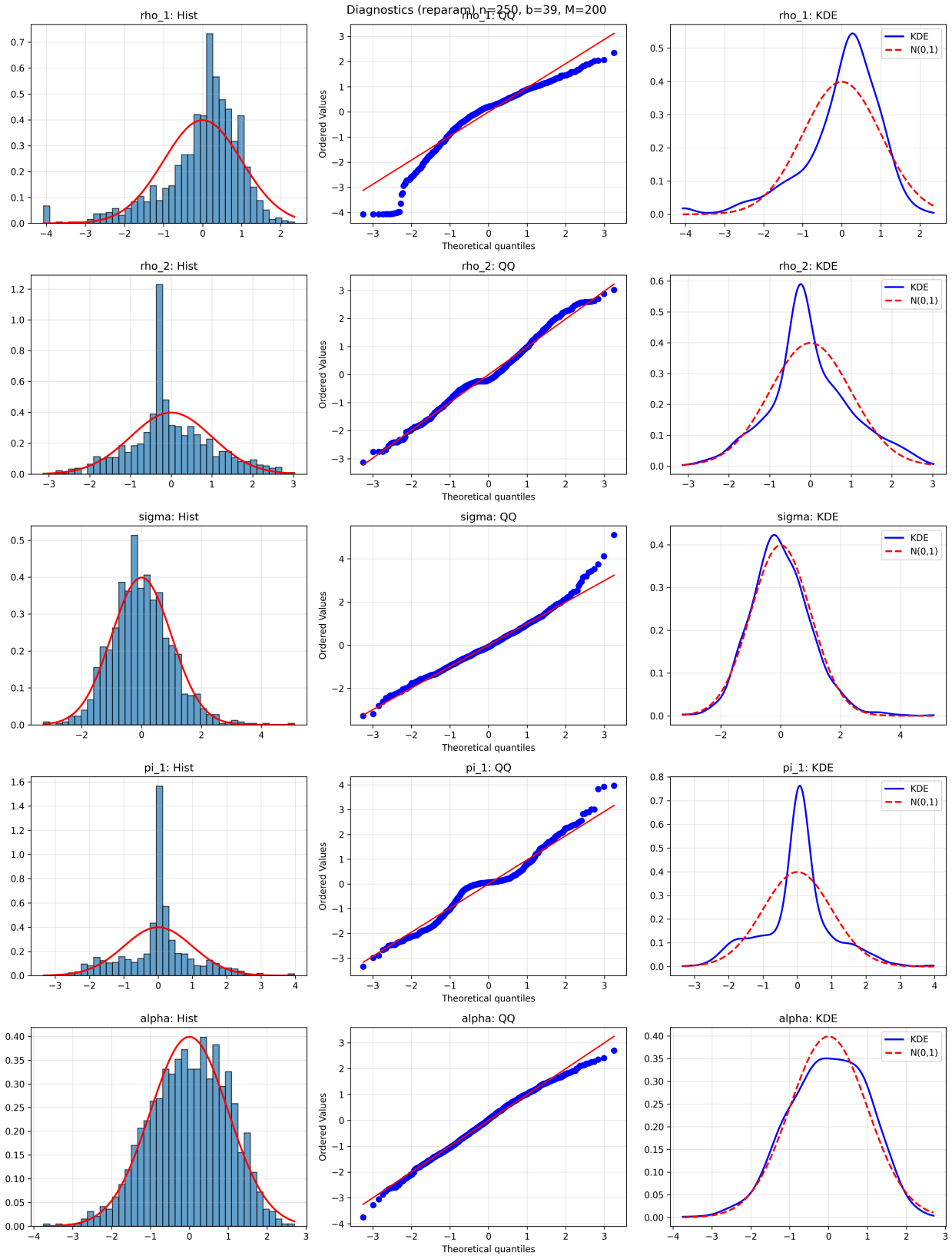

Figure S.7: Diagnostic plots for scaled subsample deviations (reparameterized) at $n = 250$. For each parameter (rows), we display: (left) histogram with standard normal overlay, (center) Q-Q plot against standard normal quantiles, and (right) kernel density estimate compared to the standard normal density. Deviations from the reference normal distribution are expected in small samples due to finite-sample effects.

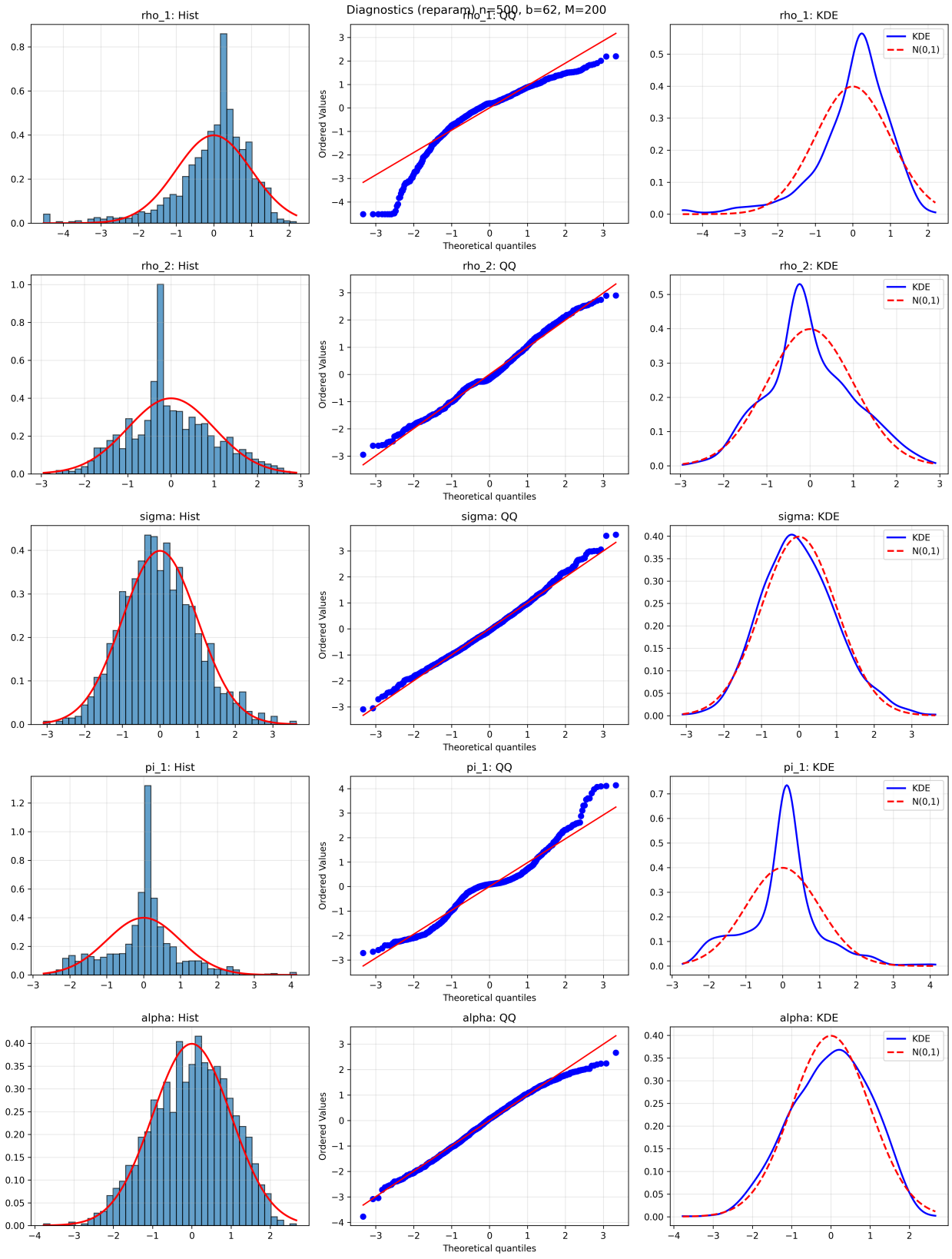

Figure S.8: Diagnostic plots for scaled subsample deviations (reparameterized) at $n = 500$. See caption to Figure S.7 for details.

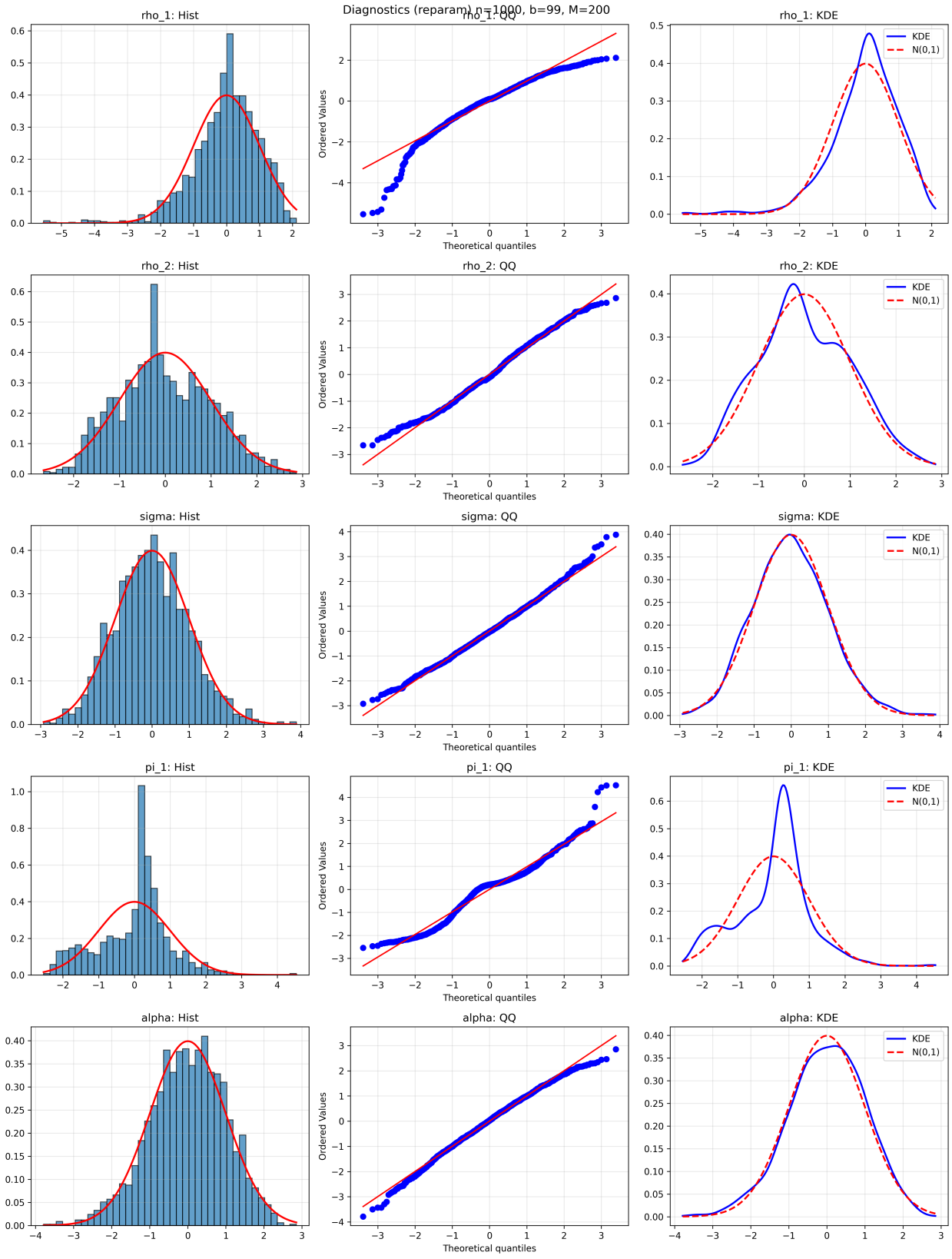

Figure S.9: Diagnostic plots for scaled subsample deviations (reparameterized) at $n = 1,000$. See caption to Figure S.7 for details.

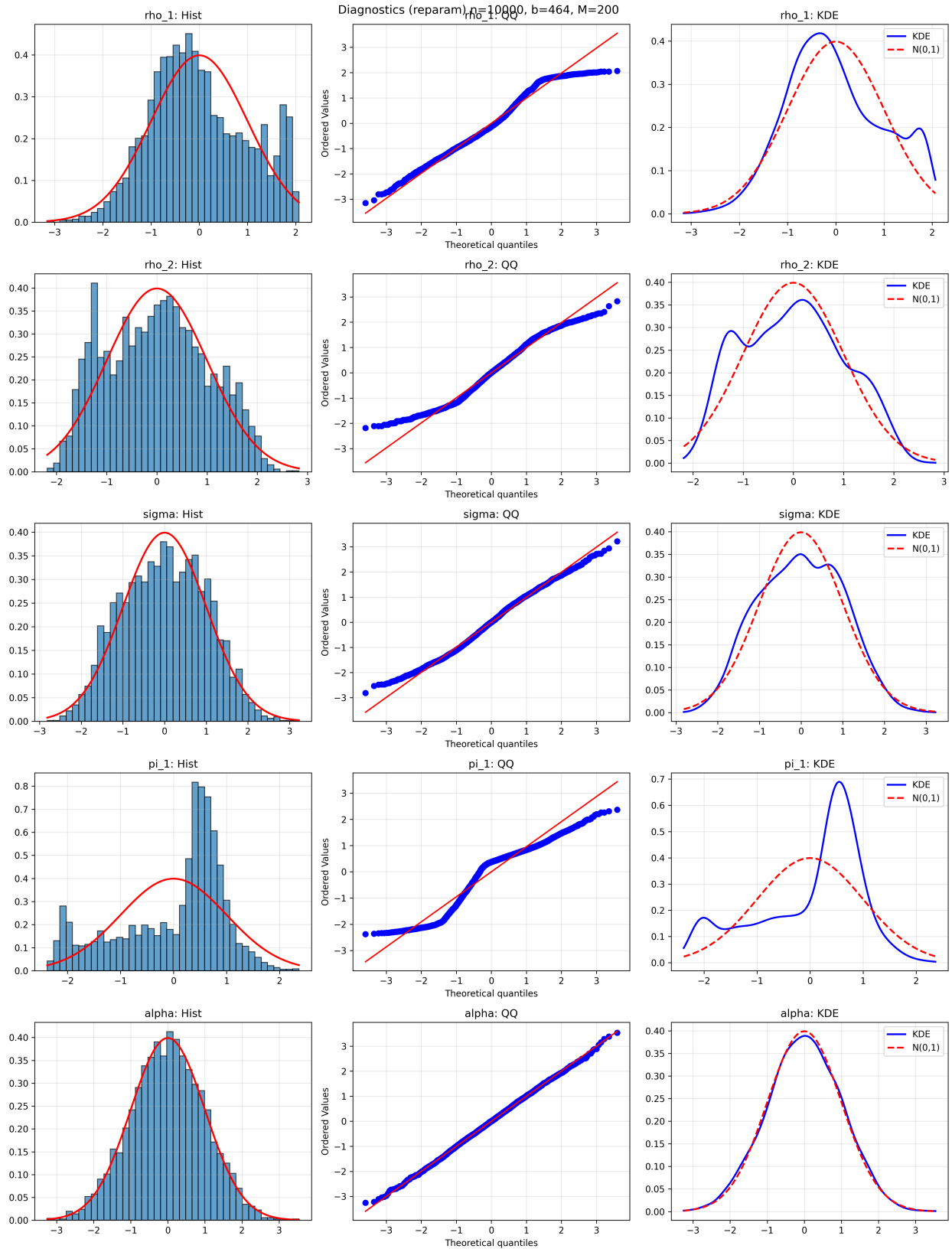

Figure S.10: Diagnostic plots for scaled subsample deviations (reparameterized) at $n = 10,000$. See caption to Figure S.7 for details.

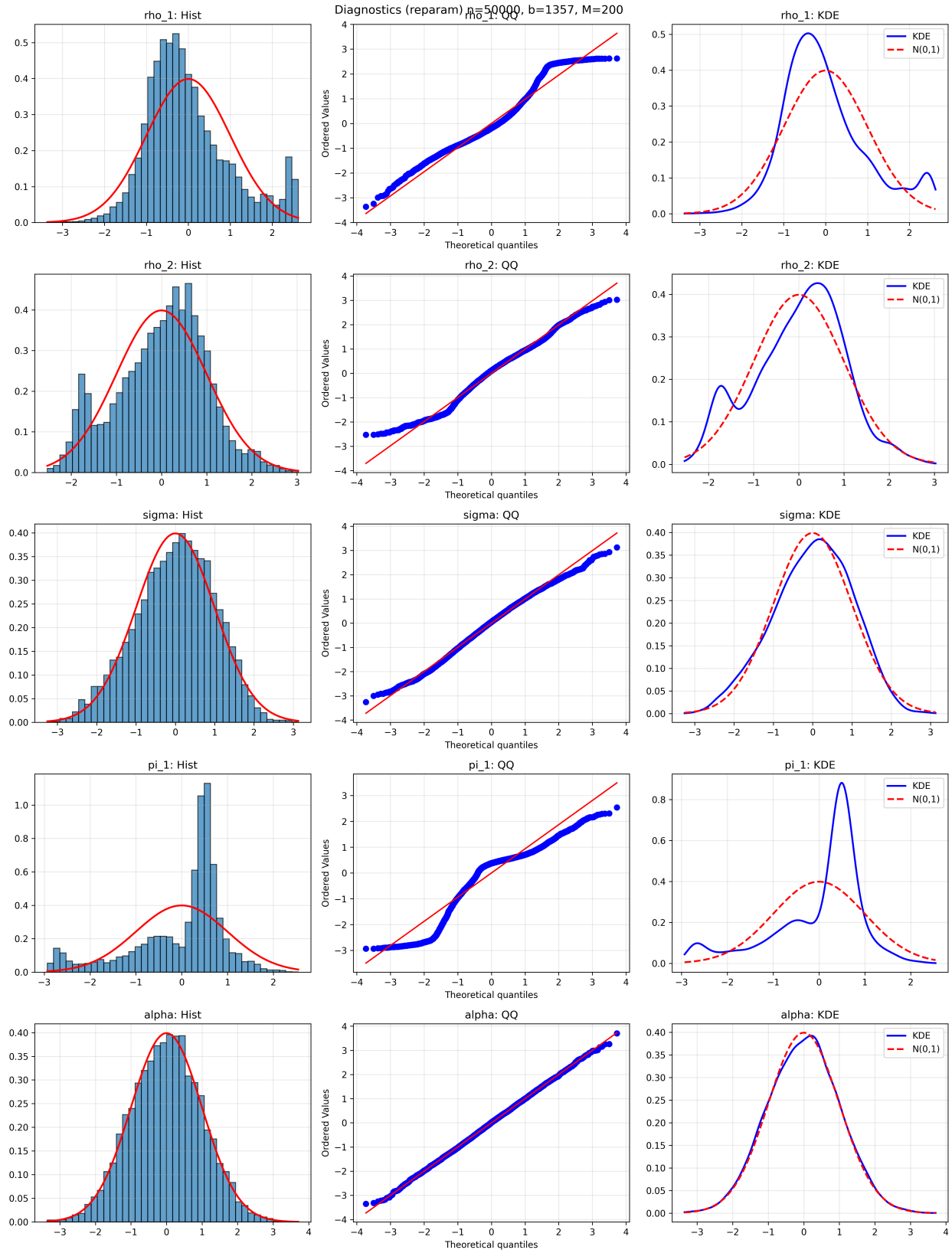

Figure S.11: Diagnostic plots for scaled subsample deviations (reparameterized) at $n = 50,000$. See caption to Figure S.7 for details.

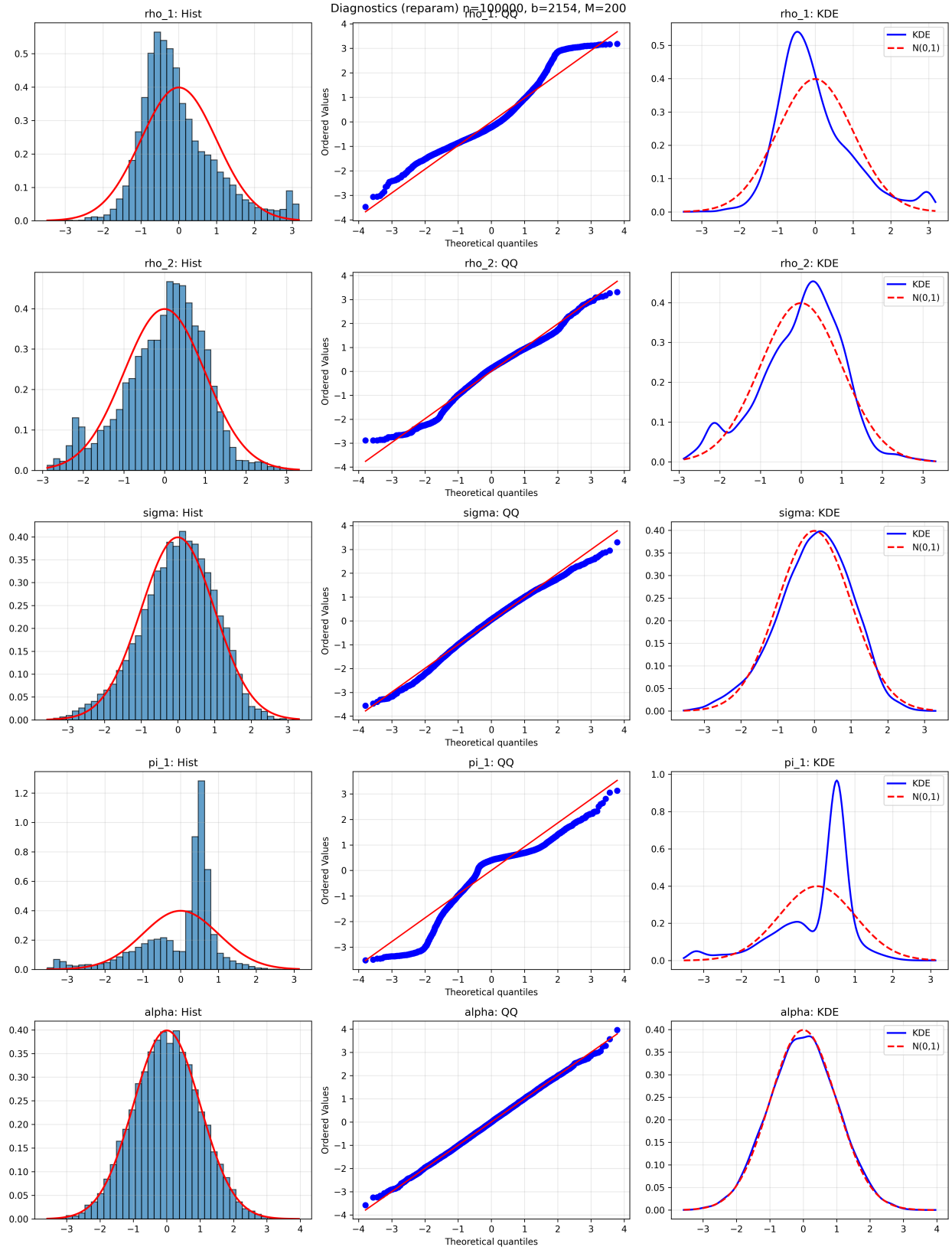

Figure S.12: Diagnostic plots for scaled subsample deviations (reparameterized) at $n = 100,000$. See caption to Figure S.7 for details. At this sample size, α and σ display near-perfect Gaussian alignment, while ρ_1, ρ_2, and π_1 retain visible departures consistent with the persistent finite-sample bias documented in Table S.16.

Table S.16: Subsampling results (reparameterized) for $n = 100,000$ ($b = 2,154$, $N_b = 46$, $M = 200$)

									Quantile CI		Normal CI		
Parameter	True	Avg Est.	Std Est.	Dev. Mean	Dev. Std	Skew	Kurt	SW Rej.	JB Rej.	qCov90	qCov95	nCov90	nCov95
ρ_1	0.800	0.778	0.013	1.105	2.944	0.889	0.847	0.780	0.635	0.145	0.155	0.155	0.170
ρ_2	0.300	0.249	0.025	1.752	5.651	−0.382	−0.018	0.360	0.050	0.175	0.200	0.170	0.205
σ	1.600	1.609	0.017	−1.483	6.013	−0.305	−0.124	0.090	0.035	0.795	0.850	0.905	0.950
π_1	0.438	0.491	0.028	−2.593	5.455	−1.251	1.427	0.995	0.885	0.145	0.155	0.145	0.145
α	1.500	1.501	0.009	−0.051	2.867	−0.004	−0.196	0.060	0.040	0.910	0.960	0.925	0.965

Notes: See notes to Table S.11.

S.2.4. Criterion difference test for $H_0 : \pi_1 = 1/2$

The poor identification of π_1 documented in Section S.2.3 raises the question of whether the mixing proportion is genuinely identified by the characteristic function-based objective. To address this formally, we implement a criterion difference test analogous to the classical likelihood ratio test in a GMM/MDE setting.

Let $\hat{\theta}_n^{\text{free}}$ denote the unrestricted MDE estimator (with π_1 free) and $\hat{\theta}_n^{\text{restr}}$ the restricted estimator imposing $\pi_1 = 1/2$ (i.e., $\varsigma_1 = \varsigma_2 = \sigma/2$). The criterion difference statistic is

$$\Delta_n = n \left[Q_n\left(\hat{\theta}_n^{\text{restr}}\right) - Q_n\left(\hat{\theta}_n^{\text{free}}\right) \right], \tag{S.4}$$

where $Q_n(\theta) = \int |\hat{\varphi}_n(s) - \varphi(s;\theta)|^2 \, w(s) \, ds$ is the MDE objective function defined in equation (2.14) of the main paper. Under H_0 and standard regularity conditions, $\Delta_n \xrightarrow{d} \chi^2(1)$. Because the flatness of the objective surface may invalidate the χ^2 approximation, we supplement the asymptotic p-value with a subsampling-based p-value. For each non-overlapping subsample $\mathcal{X}_b^{(i)}$ of size $b = \lfloor n^{2/3} \rfloor$, we compute the subsample criterion difference $\Delta_b^{(i)} = b \left[Q_b^{(i)}\left(\hat{\theta}_b^{(i),\text{restr}}\right) - Q_b^{(i)}\left(\hat{\theta}_b^{(i),\text{free}}\right) \right]$ and define the subsampling p-value as

$$\hat{p}_{\text{sub}} = \frac{1}{N_b} \sum_{i=1}^{N_b} \mathbf{1}\left\{ \Delta_b^{(i)} \geq \Delta_n \right\}. \tag{S.5}$$

We evaluate the test under the same DGP as in Sections S.2.2–S.2.3, with true parameter $\pi_1 = \varsigma_1/\sigma = 0.4375$. Since the true value is close to but not equal to $1/2$, the exercise simultaneously assesses the size of the χ^2 reference distribution and the power of the test to detect a moderate deviation from H_0. For each sample size $n \in \{500,\ 1{,}000,\ 10{,}000,\ 50{,}000,\ 100{,}000\}$, we generate $M = 200$ Monte Carlo replications. Table S.17 reports the results.

The results in Table S.17 confirm that the MDE objective is essentially flat in the π_1 direction. The mean criterion difference Δ_n remains negligible across all sample sizes, and the asymptotic $\chi^2(1)$ test never rejects H_0 at the 5% level. The subsampling-based rejection rates hover around 10%, which is consistent with the nominal size given the small number of non-overlapping blocks available at moderate sample sizes. Even at $n = 100{,}000$, the subsampling rejection rate of 17.5% remains modest, confirming that the departure from

Table S.17: Criterion difference test for $H_0\colon \pi_1 = 1/2$ (true $\pi_1 = 0.4375$, $M = 200$)

			Δ_n			Rejection rate	
n	b	M	Mean	Median	Std	$\chi^2(1)$ at 5%	Subsampling at 5%
500	62	200	0.006	0.001	0.011	0.000	0.105
1,000	99	200	0.007	0.001	0.014	0.000	0.090
10,000	464	200	0.007	0.000	0.015	0.000	0.105
50,000	1357	200	0.012	−0.001	0.029	0.000	0.175
100,000	2154	200	0.013	−0.002	0.046	0.000	0.175

Notes: $\Delta_n = n[Q_n(\hat{\theta}_n^{\text{restr}}) - Q_n(\hat{\theta}_n^{\text{free}})]$ is the criterion difference statistic defined in (S.4). The $\chi^2(1)$ column reports the fraction of replications for which the asymptotic p-value falls below 5%. The subsampling column reports the fraction for which $\hat{p}_{\text{sub}} < 0.05$. The subsample size is $b = \lfloor n^{2/3} \rfloor$.

$\pi_1 = 1/2$ (the true value being 0.4375) is essentially undetectable by the CF-based objective. These findings motivate the restricted estimation strategy adopted in the next subsection.

S.2.5. Restricted subsampling under $\pi_1 = 1/2$

As discussed in the main text, the mixing proportion π_1 is the most difficult parameter to identify from the characteristic function-based objective. A criterion difference test for $H_0\colon \pi_1 = 1/2$ confirms that the MDE objective is essentially flat in the π_1 direction, as the test never rejects H_0 at any conventional level for n up to $50,000$. Imposing $\pi_1 = 1/2$ reduces the parameter vector to $\theta_R = (\rho_1, \rho_2, \sigma, \alpha)$ and stabilizes inference on σ and α, which achieve near-nominal coverage at moderate sample sizes, at the cost of a small specification bias on (ρ_1, ρ_2) that becomes detectable at very large samples.

Table S.18: Restricted subsampling for $n = 250$ ($b = 39$, $M = 200$, $\pi_1 = 1/2$)

									Quantile CI		Normal CI		
Parameter	True	Avg Est.	Std Est.	Dev. Mean	Dev. Std	Skew	Kurt	SW Rej.	JB Rej.	qCov90	qCov95	nCov90	nCov95
ρ_1	0.800	0.713	0.116	−0.400	1.227	−0.470	−0.709	0.120	0.000	0.730	0.785	0.715	0.780
ρ_2	0.300	0.299	0.258	0.415	1.592	0.215	−0.866	0.290	0.000	0.225	0.225	0.320	0.380
σ	1.600	1.612	0.269	0.190	2.953	0.108	−0.868	0.070	0.000	0.590	0.670	0.695	0.770
α	1.500	1.492	0.157	0.309	1.993	−0.081	−0.935	0.090	0.000	0.640	0.680	0.795	0.865

Notes: See notes to Table S.11. Estimation under the restriction $\varsigma_1 = \varsigma_2 = \sigma/2$.

Table S.19: Restricted subsampling for $n = 500$ ($b = 62$, $M = 200$, $\pi_1 = 1/2$)

									Quantile CI		Normal CI		
Parameter	True	Avg Est.	Std Est.	Dev. Mean	Dev. Std	Skew	Kurt	SW Rej.	JB Rej.	qCov90	qCov95	nCov90	nCov95
ρ_1	0.800	0.728	0.118	−0.457	1.312	−0.535	−0.324	0.205	0.035	0.770	0.800	0.755	0.805
ρ_2	0.300	0.295	0.236	0.539	2.073	0.163	−0.756	0.420	0.035	0.295	0.305	0.415	0.460
σ	1.600	1.604	0.181	0.175	3.100	0.084	−0.667	0.045	0.000	0.675	0.750	0.750	0.845
α	1.500	1.497	0.109	0.289	2.323	−0.161	−0.774	0.075	0.000	0.795	0.815	0.865	0.910

Notes: See notes to Table S.18.

Table S.20: Restricted subsampling for $n = 1,000$ ($b = 99$, $M = 200$, $\pi_1 = 1/2$)

									Quantile CI		Normal CI		
Parameter	True	Avg Est.	Std Est.	Dev. Mean	Dev. Std	Skew	Kurt	SW Rej.	JB Rej.	qCov90	qCov95	nCov90	nCov95
ρ_1	0.800	0.747	0.099	−0.468	1.262	−0.491	−0.361	0.160	0.045	0.870	0.890	0.800	0.870
ρ_2	0.300	0.270	0.198	0.700	2.644	0.132	−1.028	0.550	0.025	0.320	0.325	0.475	0.580
σ	1.600	1.606	0.146	0.200	3.425	0.092	−0.458	0.055	0.010	0.695	0.745	0.755	0.820
α	1.500	1.498	0.089	0.236	2.401	−0.107	−0.596	0.045	0.010	0.800	0.810	0.830	0.885

Notes: See notes to Table S.18.

Table S.21: Restricted subsampling for $n = 10,000$ ($b = 464$, $M = 200$, $\pi_1 = 1/2$)

									Quantile CI		Normal CI		
Parameter	True	Avg Est.	Std Est.	Dev. Mean	Dev. Std	Skew	Kurt	SW Rej.	JB Rej.	qCov90	qCov95	nCov90	nCov95
ρ_1	0.800	0.773	0.011	−0.540	1.287	−0.551	0.045	0.185	0.095	0.560	0.715	0.270	0.425
ρ_2	0.300	0.239	0.056	0.873	4.877	0.332	−1.038	0.575	0.005	0.400	0.400	0.625	0.725
σ	1.600	1.609	0.044	0.242	4.153	0.166	−0.400	0.045	0.005	0.855	0.895	0.865	0.905
α	1.500	1.499	0.027	0.157	2.669	0.014	−0.361	0.050	0.020	0.890	0.915	0.895	0.925

Notes: See notes to Table S.18.

Table S.22: Restricted subsampling for $n = 50,000$ ($b = 1,357$, $M = 200$, $\pi_1 = 1/2$)

									Quantile CI		Normal CI		
Parameter	True	Avg Est.	Std Est.	Dev. Mean	Dev. Std	Skew	Kurt	SW Rej.	JB Rej.	qCov90	qCov95	nCov90	nCov95
ρ_1	0.800	0.774	0.005	−0.322	1.257	−0.632	0.814	0.335	0.320	0.000	0.015	0.000	0.000
ρ_2	0.300	0.238	0.026	0.488	5.779	0.231	−0.572	0.255	0.000	0.185	0.185	0.215	0.360
σ	1.600	1.609	0.021	0.142	4.434	0.146	−0.355	0.045	0.030	0.865	0.915	0.850	0.920
α	1.500	1.501	0.013	0.099	2.727	0.011	−0.243	0.055	0.025	0.875	0.915	0.870	0.925

Notes: See notes to Table S.18.

Table S.23: Restricted subsampling for $n = 100,000$ ($b = 2,154$, $M = 200$, $\pi_1 = 1/2$)

									Quantile CI		Normal CI		
Parameter	True	Avg Est.	Std Est.	Dev. Mean	Dev. Std	Skew	Kurt	SW Rej.	JB Rej.	qCov90	qCov95	nCov90	nCov95
ρ_1	0.800	0.774	0.003	−0.248	1.197	−0.534	0.786	0.275	0.290	0.000	0.000	0.000	0.000
ρ_2	0.300	0.240	0.018	0.353	6.069	0.087	−0.369	0.090	0.000	0.075	0.115	0.065	0.120
σ	1.600	1.610	0.014	0.113	4.609	0.090	−0.278	0.050	0.010	0.840	0.905	0.835	0.900
α	1.500	1.501	0.008	0.080	2.788	0.013	−0.199	0.065	0.040	0.935	0.955	0.940	0.975

Notes: See notes to Table S.18.

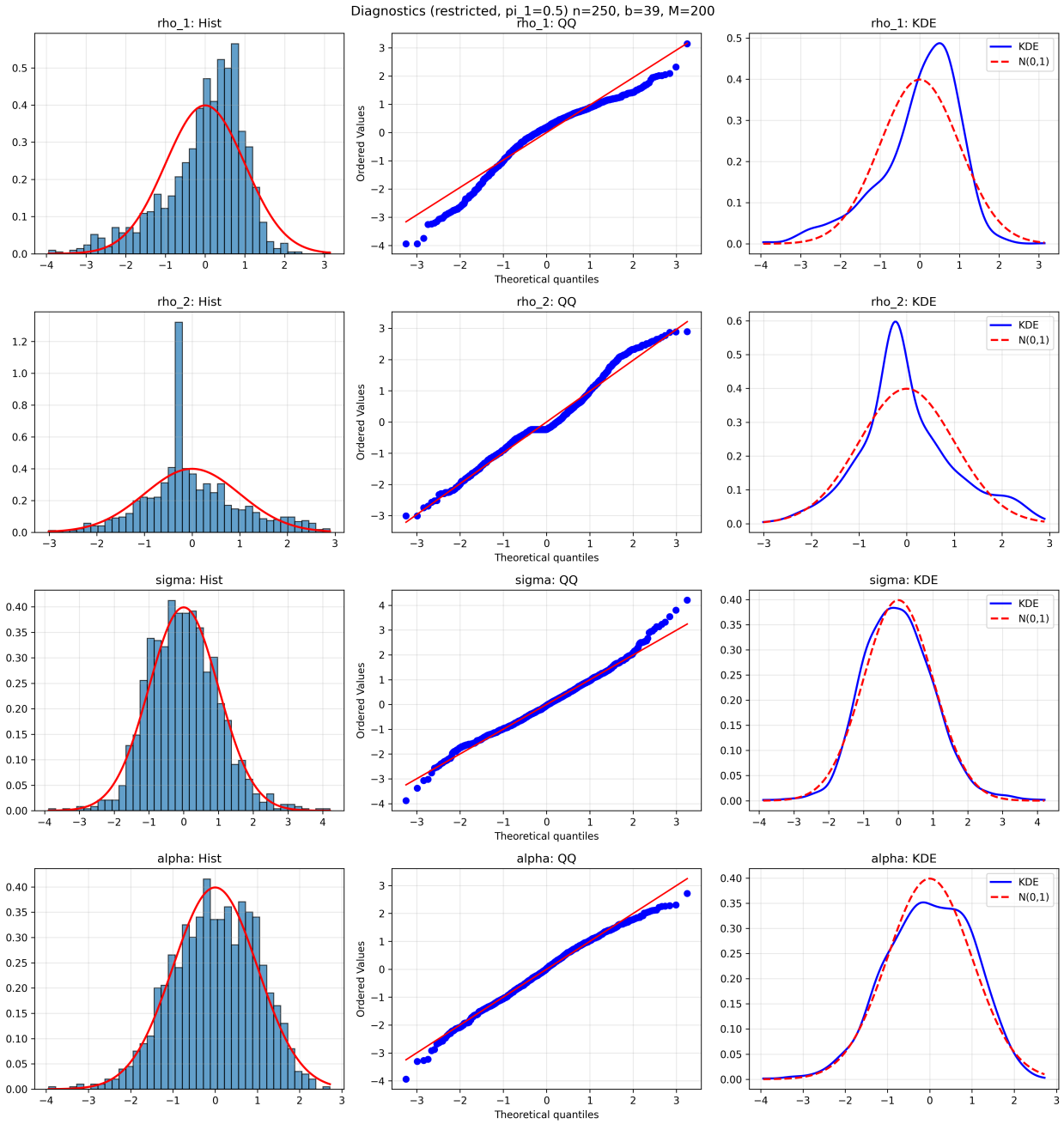

Figure S.13: Diagnostic plots for restricted subsampling ($\pi_1 = 1/2$) at $n = 250$. For each parameter (rows): histogram with standard normal overlay (left), Q-Q plot (center), and kernel density estimate vs. $\mathcal{N}(0, 1)$ (right).

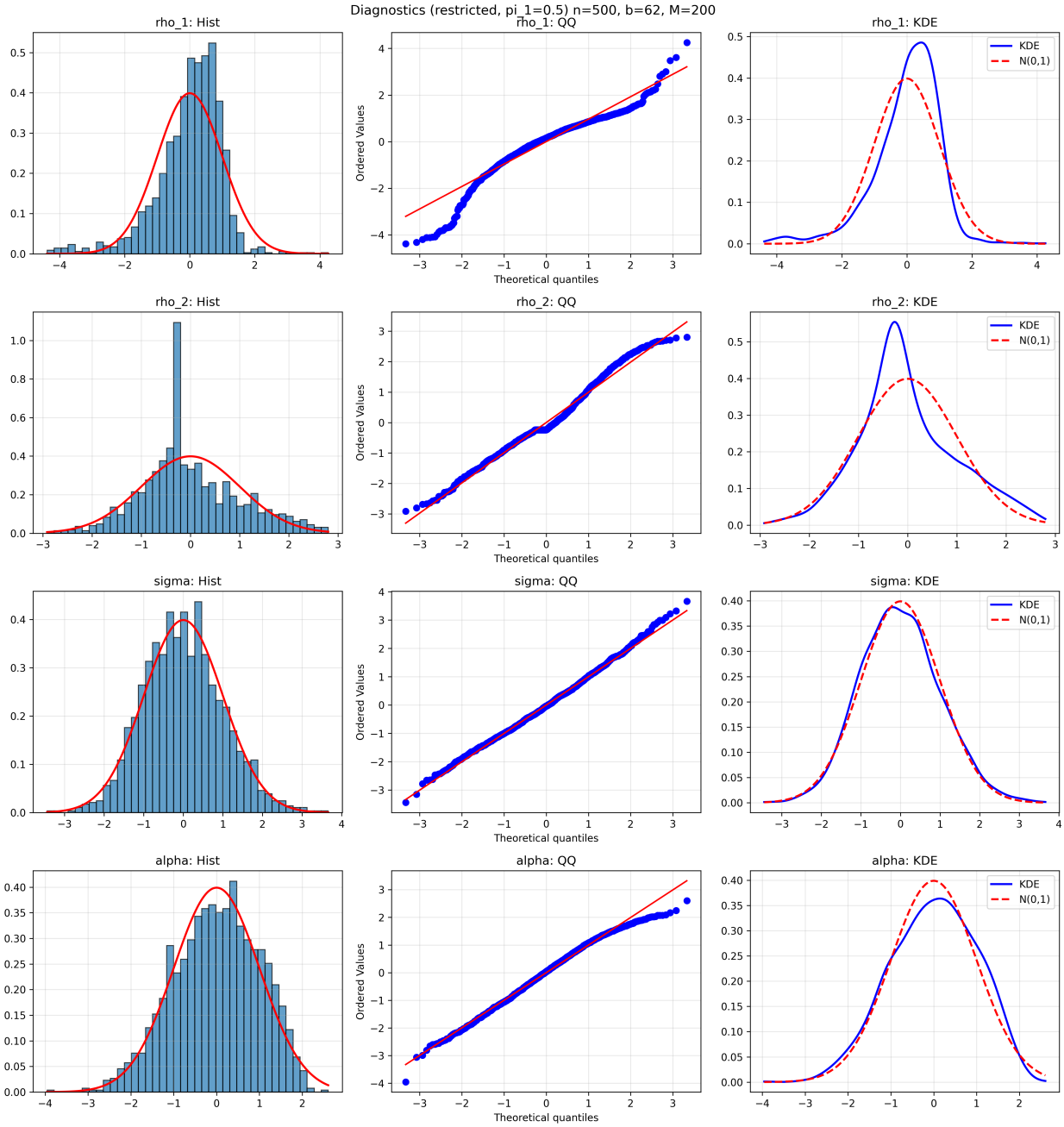

Figure S.14: Diagnostic plots for restricted subsampling ($\pi_1 = 1/2$) at $n = 500$. See caption to Figure S.13 for details.

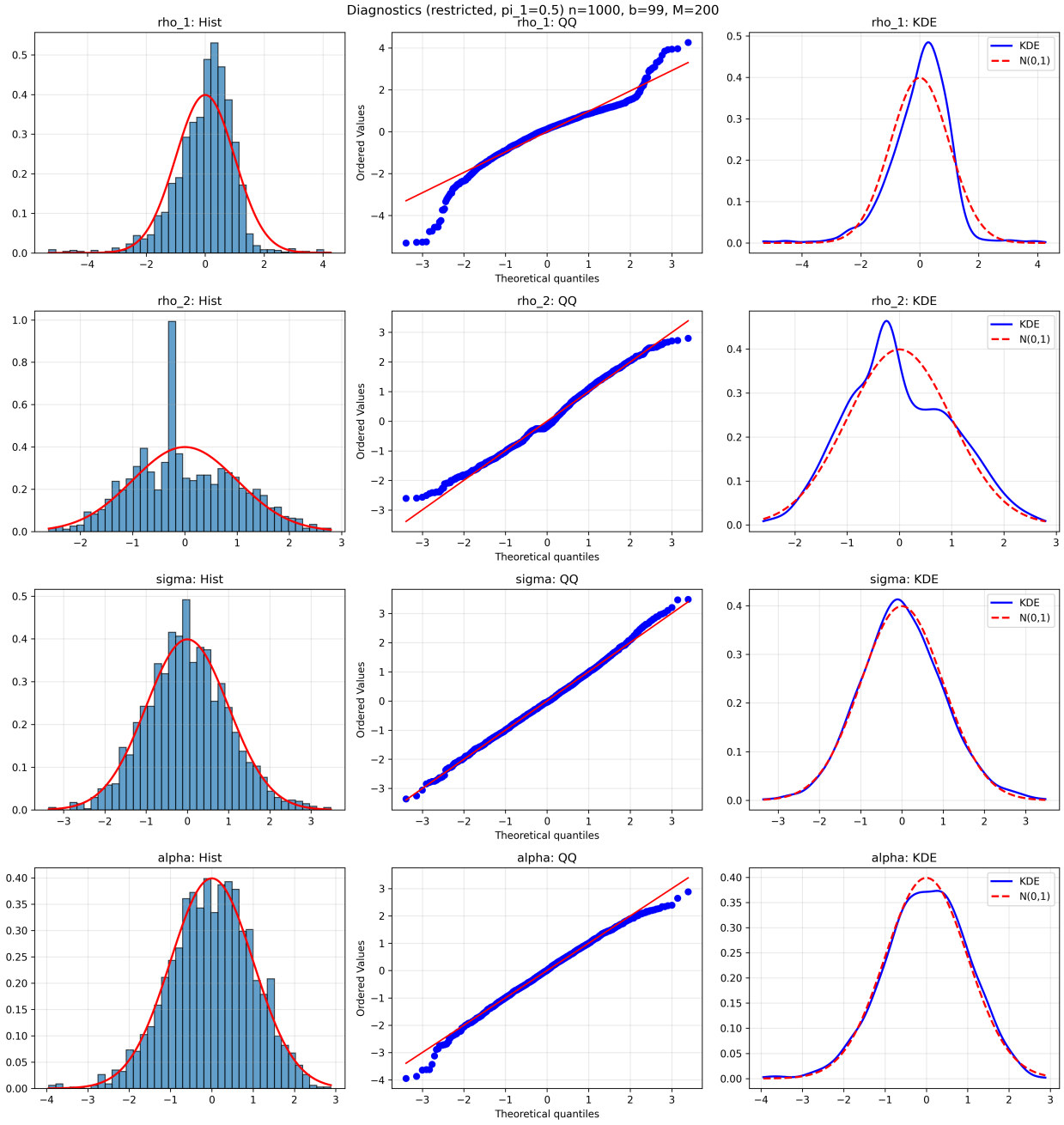

Figure S.15: Diagnostic plots for restricted subsampling ($\pi_1 = 1/2$) at $n = 1,000$. See caption to Figure S.13 for details.

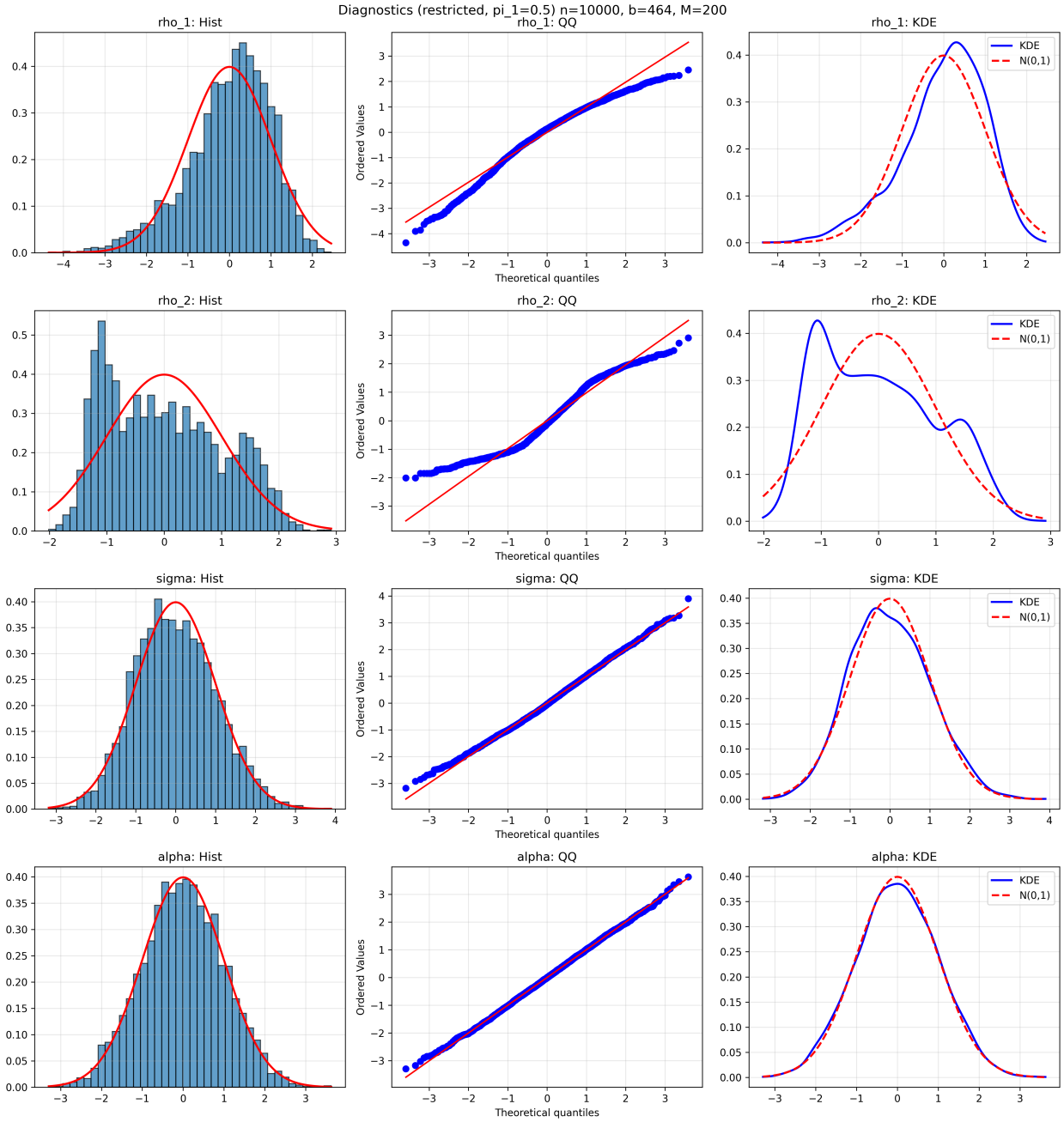

Figure S.16: Diagnostic plots for restricted subsampling ($\pi_1 = 1/2$) at $n = 10,000$. See caption to Figure S.13 for details.

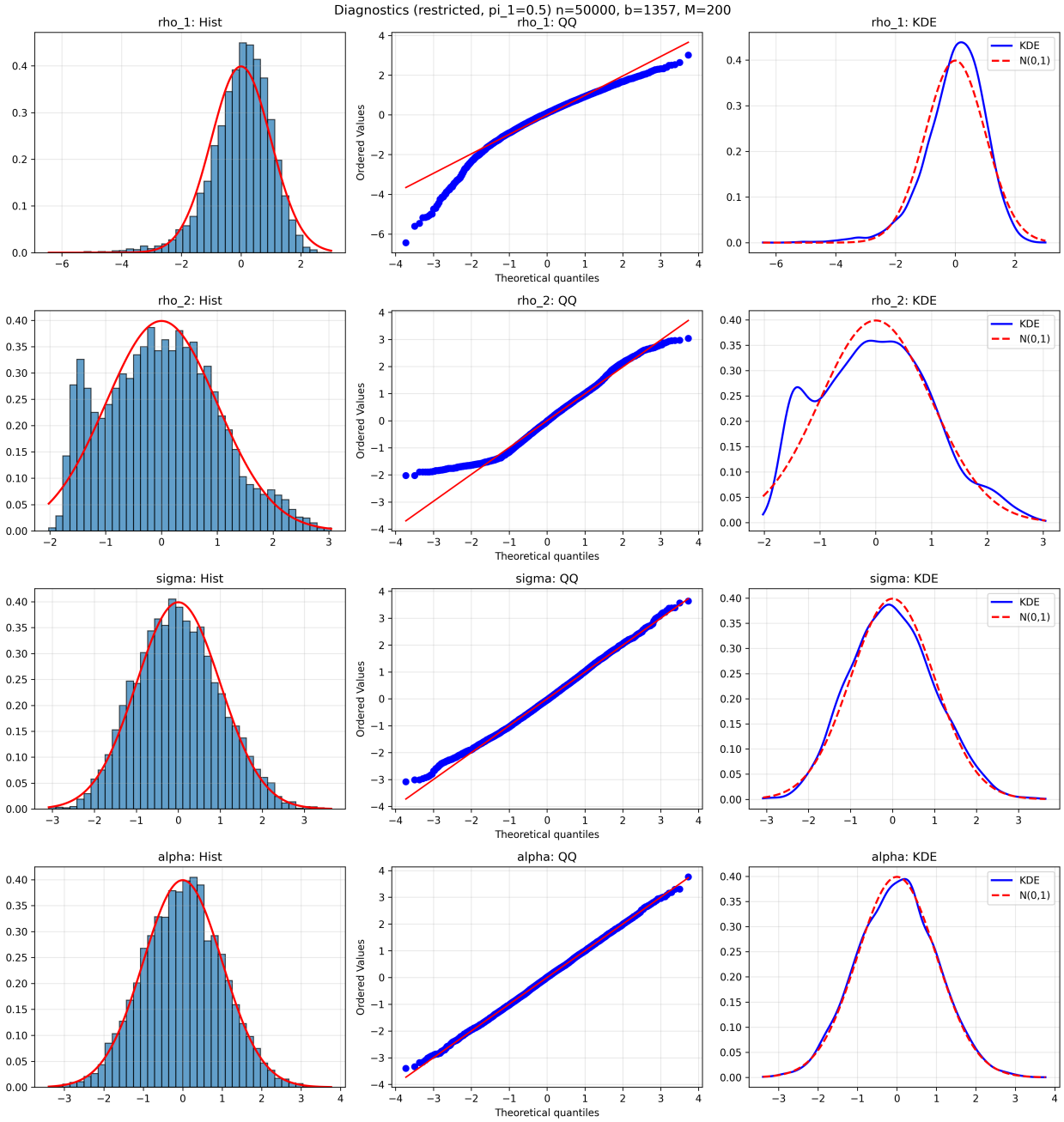

Figure S.17: Diagnostic plots for restricted subsampling ($\pi_1 = 1/2$) at $n = 50,000$. See caption to Figure S.13 for details.

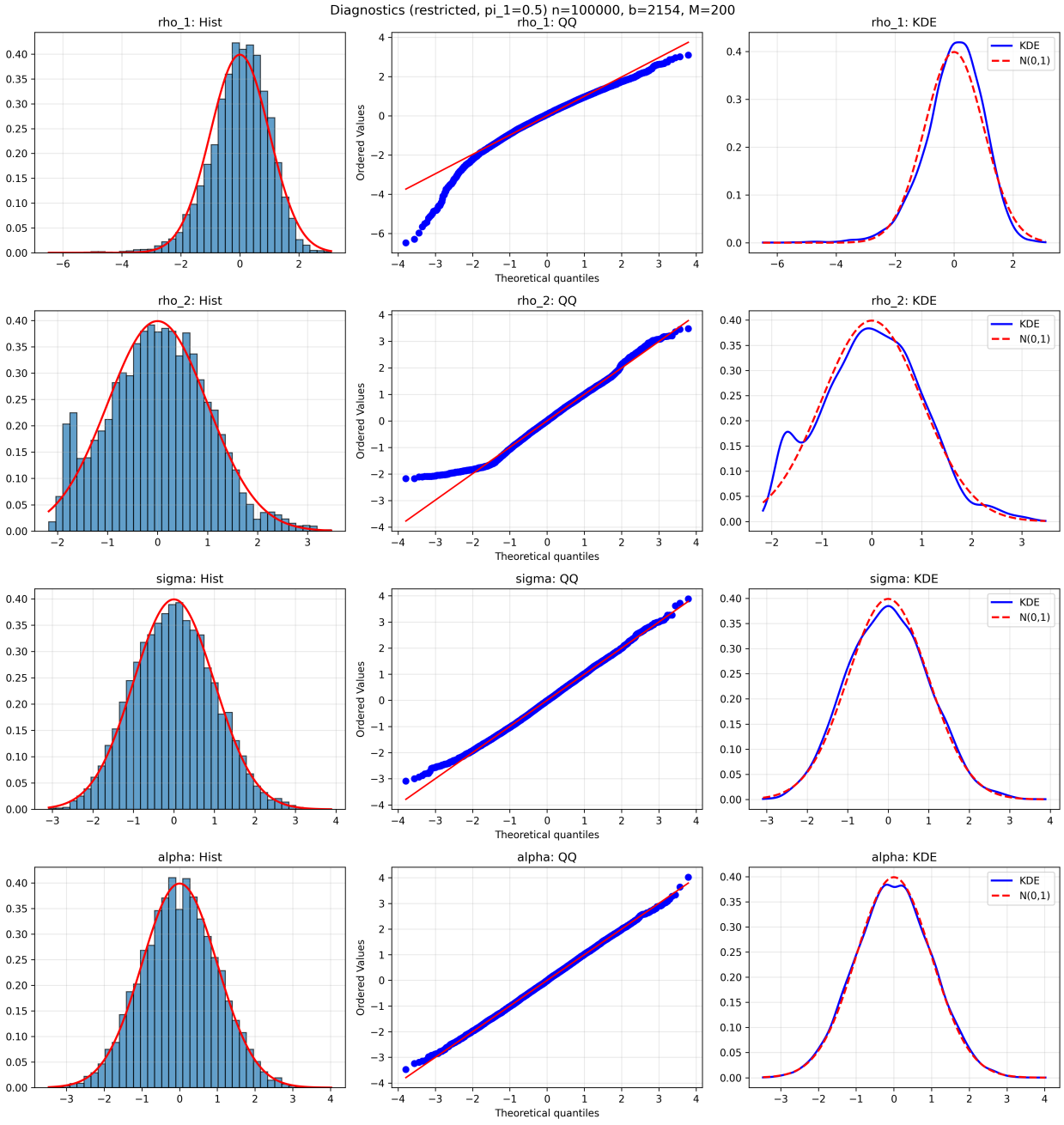

Figure S.18: Diagnostic plots for restricted subsampling ($\pi_1 = 1/2$) at $n = 100,000$. See caption to Figure S.13 for details. At this sample size, σ and α display near-perfect Gaussian alignment, while ρ_1 retains visible left skewness and a heavy left tail consistent with the specification bias induced by the constraint $\pi_1 = 1/2 \neq 0.4375$.

S.2.6. Restricted subsampling under $\pi_1 = 0.4375$ (true value)

Section S.2.5 imposed the (false) restriction $\pi_1 = 1/2$ to assess the trade-off between specification bias and estimation stability. We now complement that analysis by imposing the *true* restriction $\pi_1 = \pi_{1,0} = 0.4375$, so that the restricted parameter vector becomes $\theta_R = (\rho_1, \rho_2, \sigma, \alpha)$ under a correctly specified constraint. Since the restriction is now compatible with the data-generating process, this exercise provides a benchmark: any remaining finite-sample distortions in coverage or normality are attributable solely to the slow convergence of the subsampling approximation, not to specification bias.

Tables S.24–S.29 report the subsampling diagnostics for $n \in \{250,\ 500,\ 1,000,\ 10,000,\ 50,000\ 100,000\}$, and Figures S.19–S.24 display the corresponding graphical diagnostics.

Table S.24: Restricted subsampling for $n = 250$ ($b = 39$, $M = 200$, $\pi_1 = 0.4375$)

									Quantile CI		Normal CI		
Parameter	True	Avg Est.	Std Est.	Dev. Mean	Dev. Std	Skew	Kurt	SW Rej.	JB Rej.	qCov90	qCov95	nCov90	nCov95
ρ_1	0.800	0.730	0.138	−0.411	1.226	−0.434	−0.734	0.130	0.000	0.640	0.695	0.715	0.790
ρ_2	0.300	0.327	0.249	0.280	1.660	0.121	−0.898	0.250	0.000	0.205	0.220	0.360	0.430
σ	1.600	1.594	0.276	0.151	2.936	0.095	−0.863	0.060	0.000	0.570	0.635	0.685	0.775
α	1.500	1.489	0.158	0.302	2.005	−0.078	−0.938	0.090	0.000	0.640	0.685	0.790	0.870

Notes: All results are in the reparameterized space $(\rho_1, \rho_2, \sigma, \alpha)$ under the true restriction $\pi_1 = 0.4375$. SW and JB rejection rates are at the 5% level. qCov and nCov denote quantile-based and normal-approximation CI coverage. Confidence intervals are constructed from thinned overlapping blocks; normality diagnostics use non-overlapping blocks.

Table S.25: Restricted subsampling for $n = 500$ ($b = 62$, $M = 200$, $\pi_1 = 0.4375$)

									Quantile CI		Normal CI		
Parameter	True	Avg Est.	Std Est.	Dev. Mean	Dev. Std	Skew	Kurt	SW Rej.	JB Rej.	qCov90	qCov95	nCov90	nCov95
ρ_1	0.800	0.751	0.130	−0.469	1.313	−0.576	−0.329	0.185	0.035	0.690	0.750	0.805	0.835
ρ_2	0.300	0.329	0.217	0.317	2.099	0.120	−0.807	0.375	0.035	0.295	0.315	0.475	0.540
σ	1.600	1.590	0.185	0.116	3.098	0.083	−0.671	0.045	0.000	0.660	0.720	0.740	0.820
α	1.500	1.494	0.110	0.283	2.337	−0.156	−0.787	0.070	0.000	0.780	0.810	0.860	0.910

Notes: See notes to Table S.24.

Table S.26: Restricted subsampling for $n = 1,000$ ($b = 99$, $M = 200$, $\pi_1 = 0.4375$)

									Quantile CI		Normal CI		
Parameter	True	Avg Est.	Std Est.	Dev. Mean	Dev. Std	Skew	Kurt	SW Rej.	JB Rej.	qCov90	qCov95	nCov90	nCov95
ρ_1	0.800	0.761	0.131	−0.513	1.324	−0.491	−0.344	0.170	0.060	0.750	0.780	0.860	0.885
ρ_2	0.300	0.321	0.190	0.424	2.583	0.052	−1.075	0.405	0.010	0.370	0.375	0.510	0.595
σ	1.600	1.594	0.151	0.124	3.438	0.092	−0.466	0.070	0.010	0.680	0.740	0.750	0.810
α	1.500	1.496	0.090	0.222	2.410	−0.108	−0.607	0.045	0.010	0.800	0.820	0.825	0.880

Notes: See notes to Table S.24.

Table S.27: Restricted subsampling for $n = 10,000$ ($b = 464$, $M = 200$, $\pi_1 = 0.4375$)

									Quantile CI		Normal CI		
Parameter	True	Avg Est.	Std Est.	Dev. Mean	Dev. Std	Skew	Kurt	SW Rej.	JB Rej.	qCov90	qCov95	nCov90	nCov95
ρ_1	0.800	0.799	0.010	−0.599	1.412	−0.704	0.191	0.295	0.165	0.890	0.920	0.965	0.980
ρ_2	0.300	0.298	0.050	0.369	4.693	0.131	−1.036	0.280	0.000	0.775	0.775	0.865	0.920
σ	1.600	1.599	0.044	0.093	4.287	0.141	−0.437	0.045	0.010	0.830	0.880	0.860	0.925
α	1.500	1.498	0.028	0.123	2.707	0.006	−0.359	0.050	0.020	0.880	0.915	0.895	0.925

Notes: See notes to Table S.24.

Table S.28: Restricted subsampling for $n = 50{,}000$ ($b = 1{,}357$, $M = 200$, $\pi_1 = 0.4375$)

									Quantile CI		Normal CI		
Parameter	True	Avg Est.	Std Est.	Dev. Mean	Dev. Std	Skew	Kurt	SW Rej.	JB Rej.	qCov90	qCov95	nCov90	nCov95
ρ_1	0.800	0.799	0.005	−0.341	1.342	−0.819	1.190	0.435	0.390	0.905	0.925	0.935	0.965
ρ_2	0.300	0.298	0.025	0.104	5.371	0.055	−0.410	0.045	0.005	0.910	0.940	0.875	0.935
σ	1.600	1.600	0.022	0.019	4.541	0.119	−0.351	0.030	0.020	0.875	0.920	0.890	0.920
α	1.500	1.500	0.013	0.066	2.763	0.007	−0.242	0.055	0.025	0.870	0.915	0.860	0.905

Notes: See notes to Table S.24.

Table S.29: Restricted subsampling for $n = 100{,}000$ ($b = 2{,}154$, $M = 200$, $\pi_1 = 0.4375$)

									Quantile CI		Normal CI		
Parameter	True	Avg Est.	Std Est.	Dev. Mean	Dev. Std	Skew	Kurt	SW Rej.	JB Rej.	qCov90	qCov95	nCov90	nCov95
ρ_1	0.800	0.800	0.003	−0.254	1.257	−0.768	1.430	0.445	0.405	0.920	0.955	0.950	0.980
ρ_2	0.300	0.301	0.017	0.043	5.484	−0.011	−0.107	0.030	0.005	0.925	0.975	0.900	0.980
σ	1.600	1.601	0.014	0.019	4.677	0.072	−0.211	0.040	0.015	0.885	0.935	0.895	0.945
α	1.500	1.500	0.008	0.056	2.822	0.010	−0.191	0.065	0.040	0.920	0.960	0.940	0.965

Notes: See notes to Table S.24.

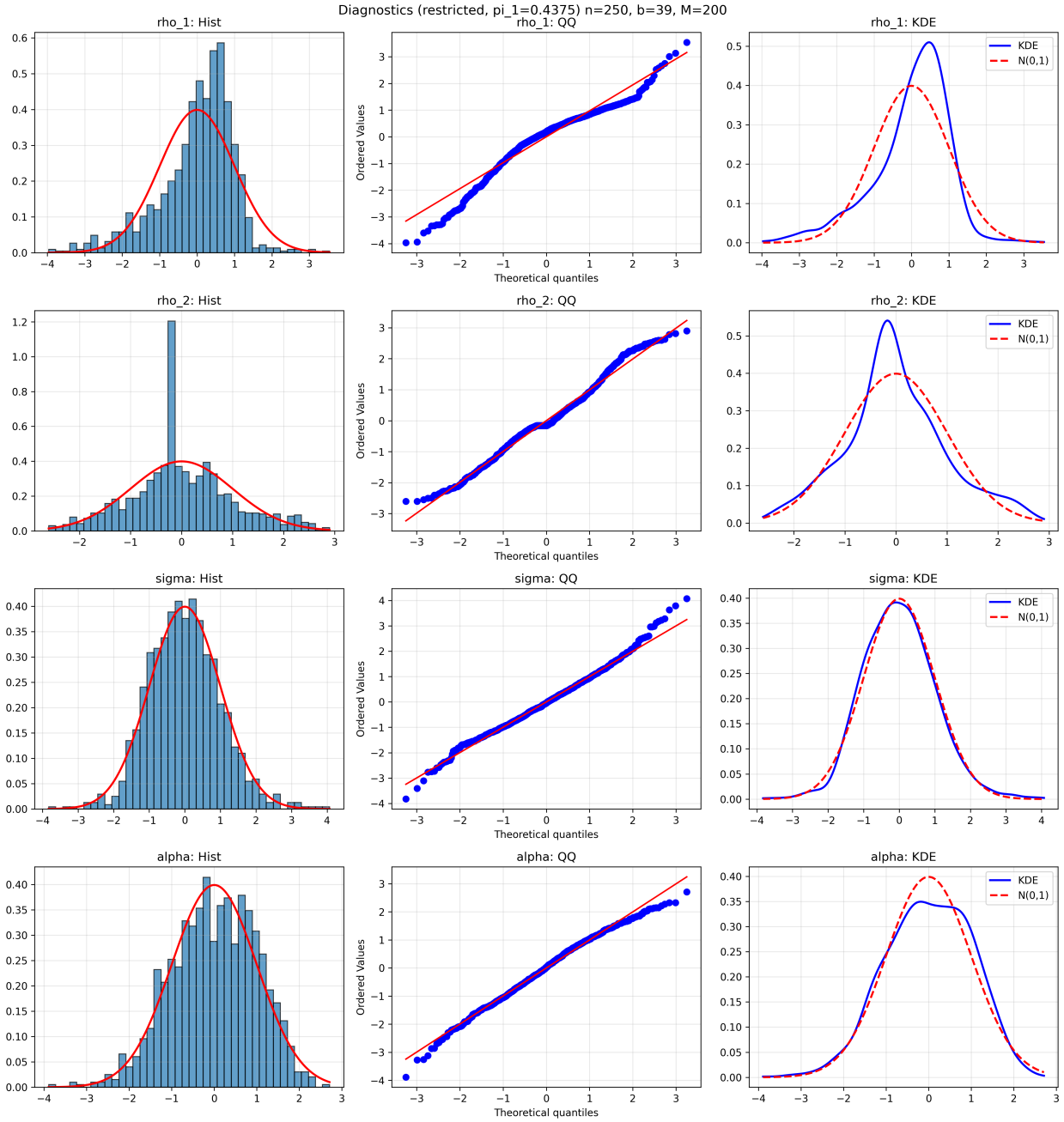

Figure S.19: Diagnostic plots for restricted subsampling ($\pi_1 = 0.4375$) at $n = 250$. For each parameter (rows): histogram with standard normal overlay (left), Q-Q plot (center), and kernel density estimate vs. $\mathcal{N}(0, 1)$ (right).

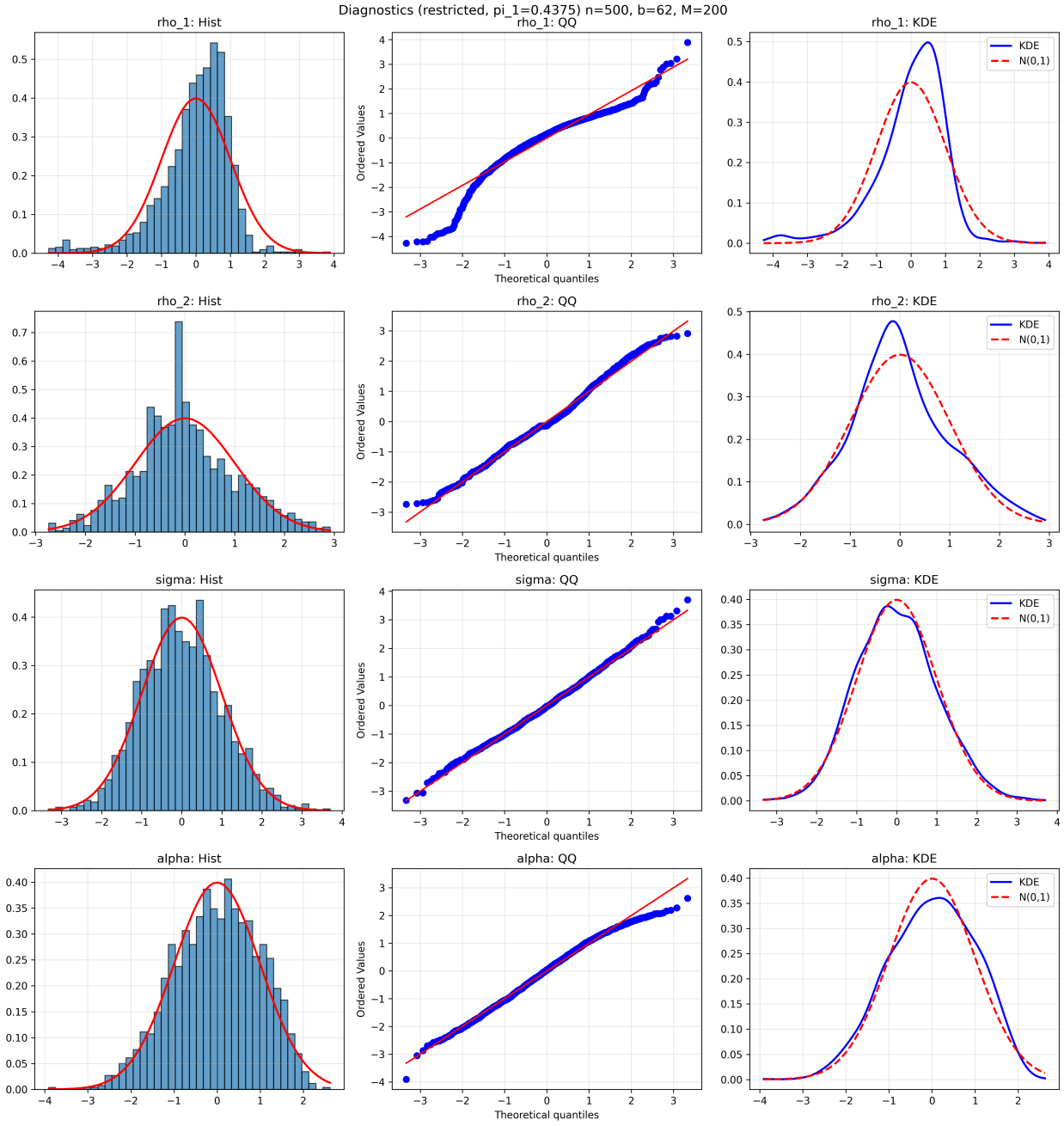

Figure S.20: Diagnostic plots for restricted subsampling ($\pi_1 = 0.4375$) at $n = 500$. See caption to Figure S.19 for details.

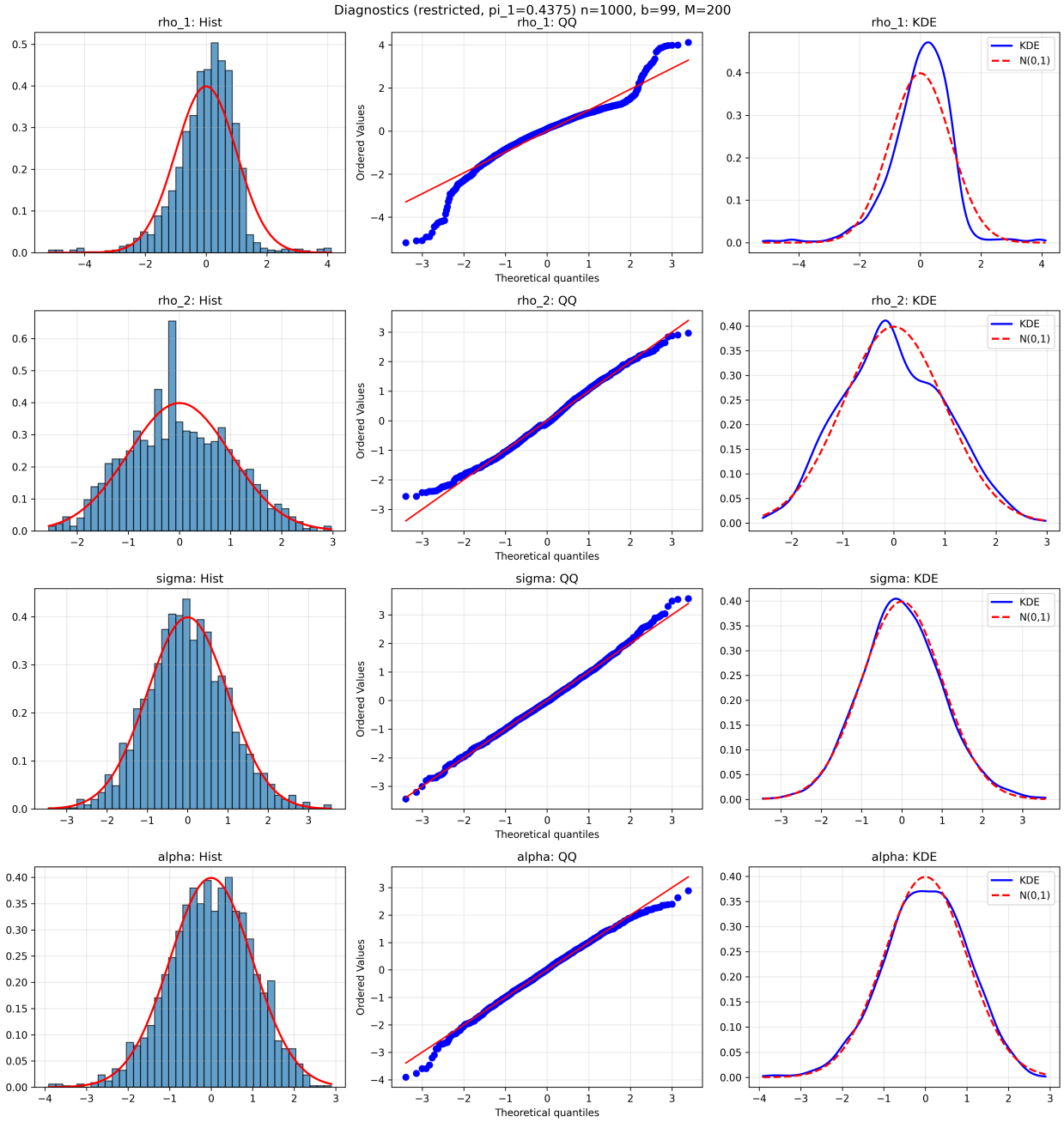

Figure S.21: Diagnostic plots for restricted subsampling ($\pi_1 = 0.4375$) at $n = 1,000$. See caption to Figure S.19 for details.

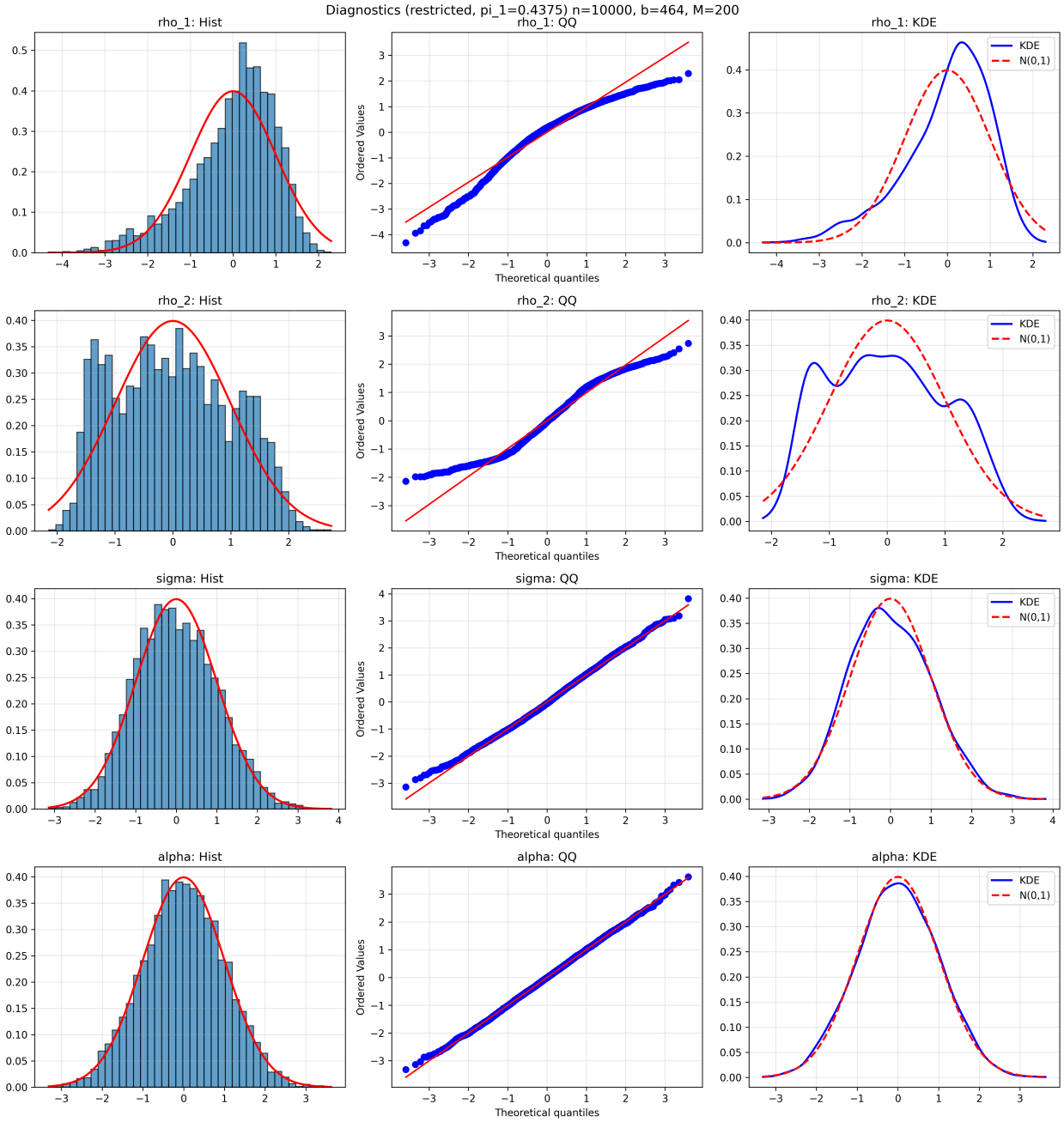

Figure S.22: Diagnostic plots for restricted subsampling ($\pi_1 = 0.4375$) at $n = 10,000$. See caption to Figure S.19 for details. .

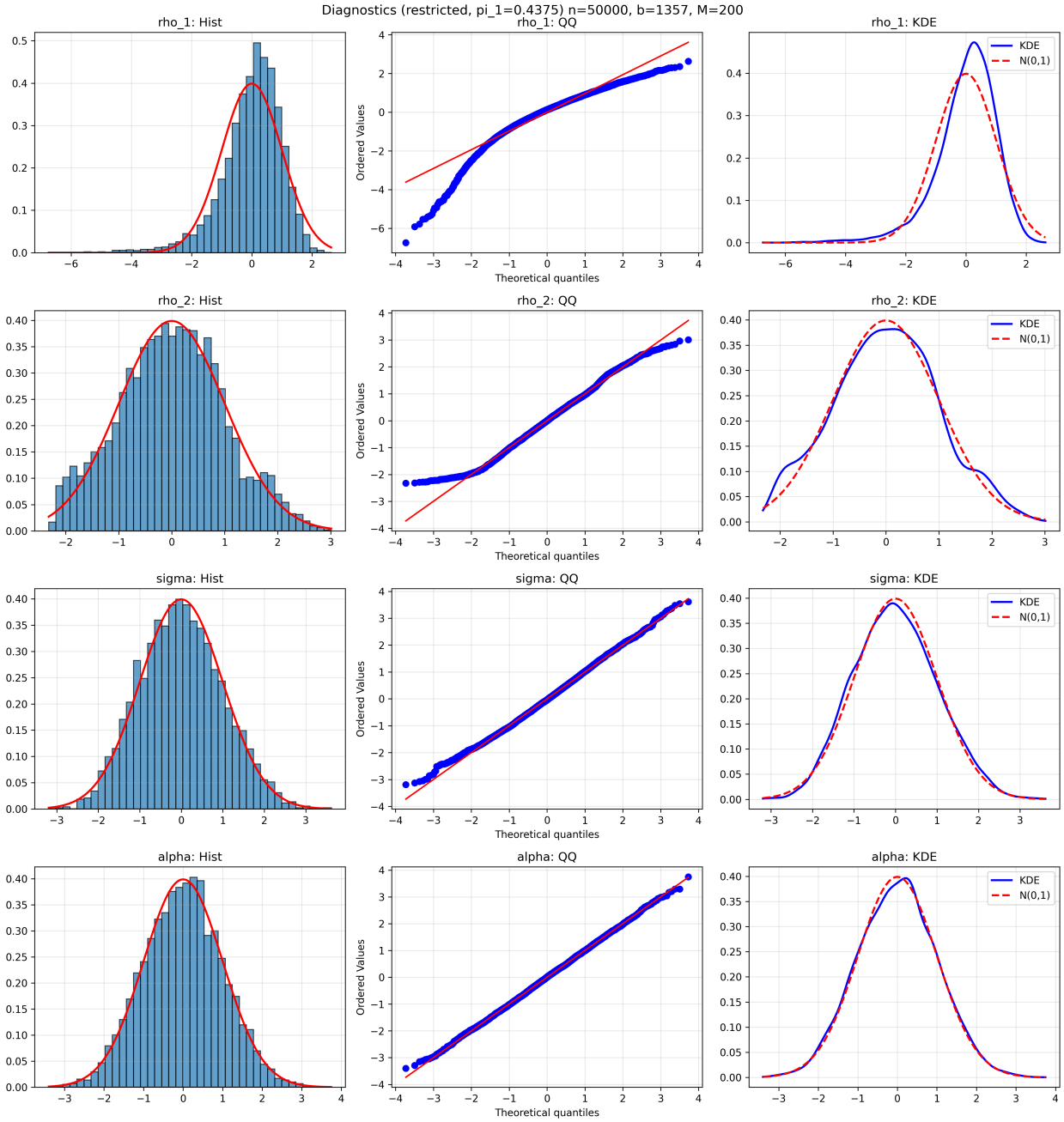

Figure S.23: Diagnostic plots for restricted subsampling ($\pi_1 = 0.4375$) at $n = 50{,}000$. See caption to Figure S.19 for details.

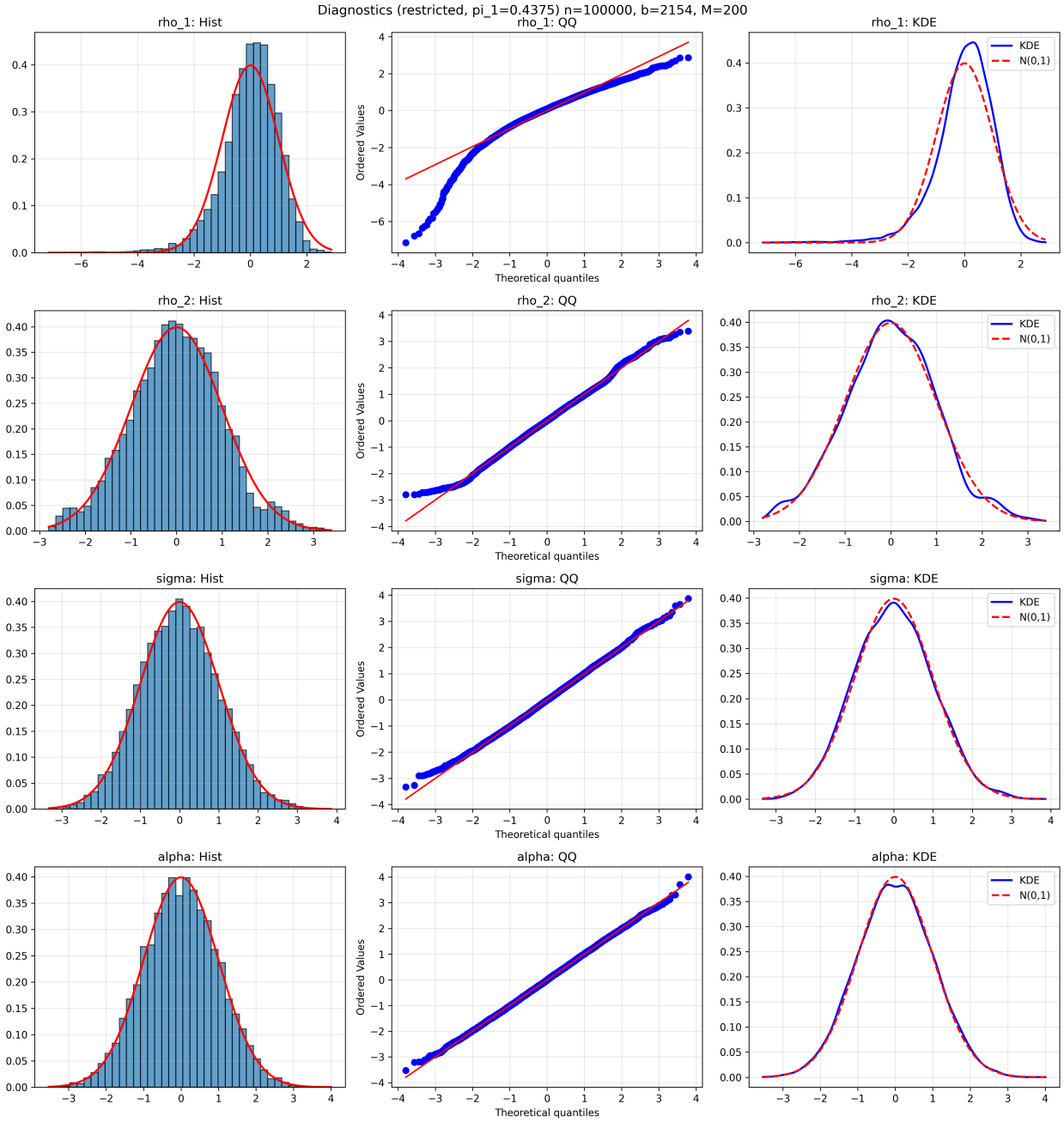

Figure S.24: Diagnostic plots for restricted subsampling ($\pi_1 = 0.4375$) at $n = 100{,}000$. See caption to Figure S.19 for details.

S.3. Application to the OVX Index

This section provides the complete empirical analysis of the CBOE Crude Oil ETF Volatility Index (OVX) that supports the summary presented in Section 5 of the main paper. The analysis proceeds in four stages. Section S.3.1 reports the estimation results under three distributional specifications and discusses the identification of the latent components. Section S.3.2 presents the deconvolution of the observed series into its two constituent components using the filtering methodology of de Truchis et al. (2025b), revealing the heterogeneous dynamics that characterize oil market volatility. Section S.3.3 develops the in-sample forecasting exercise for the 2020 oil market disruption, detailing the pattern-matching algorithm, the crash probability computations, and the role of risk thresholds in generating predictions. Section S.3.4 collects the per-component graphical diagnostics, including crash probability profiles and forecast trajectories across multiple risk thresholds.

S.3.1. Estimation

This subsection reports the minimum distance estimation results for the OVX index under three distributional specifications: general α-stable ($\mathcal{G}\alpha\mathcal{S}$), symmetric α-stable ($\mathcal{S}\alpha\mathcal{S}$), and Cauchy ($\mathcal{S}1\mathcal{S}$). The observed series is the CBOE Crude Oil ETF Volatility Index, collected from the FRED website at a weekly frequency over the period May 23, 2015–May 23, 2025 ($T = 522$), and linearly detrended to avoid high-frequency noise contamination. Table S.30 presents the parameter estimates, asymptotic standard errors computed using the subsampling methodology of the previous section, and t-statistics for each specification.

Table S.30: Estimation results for the OVX index under three specifications

	$\mathcal{G}\alpha\mathcal{S}$			$\mathcal{S}\alpha\mathcal{S}$			$\mathcal{S}1\mathcal{S}$		
$\widehat{\theta}$	Estimate	Std.	t-stat	Estimate	Std.	t-stat	Estimate	Std.	t-stat
ψ_1	0.7989	0.0673	11.862	0.2507	0.0077	32.477	0.9226	0.0082	112.824
ψ_2	0.8470	0.0668	12.678	0.9865	0.0040	244.560	0.9346	0.0074	126.404
α	1.4686	0.0995	14.764	1.2405	0.0084	147.613	–	–	–
β	−0.1275	0.0684	−1.863	–	–	–	–	–	–
σ	2.0932	0.2400	8.723	0.8964	0.0212	42.226	0.1966	0.0294	6.692
π_1	0.2790	0.0403	6.930	0.8915	0.0052	171.084	0.5029	0.0511	9.833
π_2	0.7210	0.0409	17.622	0.1085	0.0182	5.957	0.4971	0.0545	9.121

Notes: Asymptotic standard errors are computed using the subsampling methodology described in the previous section. The t-statistics test the null hypothesis that each parameter equals zero. For the $\mathcal{S}1\mathcal{S}$ specification, $\alpha = 1$ is imposed.

The $\mathcal{G}\alpha\mathcal{S}$ specification provides strong evidence of anticipative dynamics: both AR coefficients are highly significant ($\hat{\psi}_1 = 0.80$, $\hat{\psi}_2 = 0.85$), and the two latent components are clearly differentiated. The first component captures more abrupt volatility bursts (lower weight $\hat{\pi}_1 = 0.28$), while the second drives more persistent explosive episodes ($\hat{\pi}_2 = 0.72$). The estimated tail index $\hat{\alpha} = 1.47$ confirms the presence of heavy

tails well beyond Gaussian accommodation. The asymmetry parameter $\hat{\beta} = -0.13$ is not significant at the 5% level, yet numerically distorts the parameter structure of the $\mathcal{S}\alpha\mathcal{S}$ model considerably ($\hat{\psi}_1 = 0.25$, $\hat{\psi}_2 = 0.99$). The $\mathcal{S}1\mathcal{S}$ Cauchy restriction ($\alpha = 1$) appears overly binding given the estimated $\hat{\alpha}$ values in the other specifications.

S.3.2. Filtration and deconvolution

This subsection presents the deconvolution of the OVX index into its two latent components under the $\mathcal{G}\alpha\mathcal{S}$ specification. The filtering is performed using the dual MCMC procedure of de Truchis et al. (2025b), which recovers the unobserved component trajectories from the aggregate signal. Figure S.25 displays the observed detrended series alongside the filtered components.

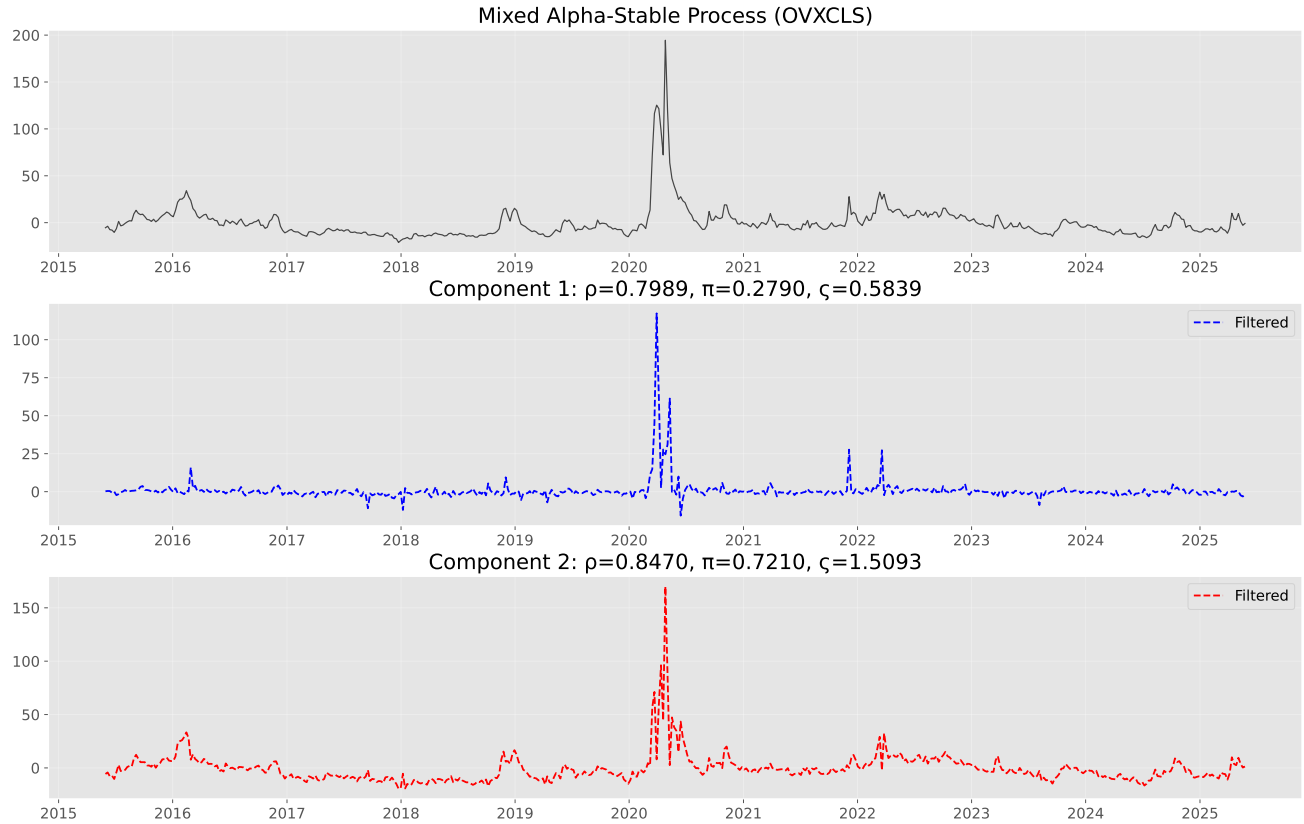

Figure S.25: Deconvolution of the OVX index from the $\mathcal{G}\alpha\mathcal{S}$ two-component model, filtered using de Truchis et al. (2025b). Top panel: observed detrended OVX series. Middle panel: filtered first component ($\hat{\psi}_1 = 0.7989$, $\hat{\pi}_1 = 0.2790$). Bottom panel: filtered second component ($\hat{\psi}_2 = 0.8470$, $\hat{\pi}_2 = 0.7210$).

The two components exhibit clearly differentiated roles. The first component captures abrupt, short-lived volatility bursts: its trajectory shows sharp spikes that decay rapidly, consistent with its lower persistence ($\hat{\psi}_1 = 0.80$) and smaller contribution to the aggregate ($\hat{\pi}_1 = 0.28$). The second component tracks more sustained explosive patterns: its evolution is smoother but more persistent, reflecting its higher autoregressive

coefficient ($\hat{\psi}_2 = 0.85$) and dominant weight ($\hat{\pi}_2 = 0.72$).

Periods of extreme oil market stress, most visibly the 2020 disruption triggered by the COVID-19 pandemic and the Russia-Saudi Arabia oil price war, feature a superposition of both dynamics. During this episode, both components contribute substantially to the observed volatility spike, but with different temporal profiles: the first component captures the initial shock and rapid escalation, while the second sustains the elevated volatility over a longer period. This heterogeneity in persistence properties is precisely what motivates our aggregate modeling framework and enables more nuanced forecasting relative to single-component approaches.

S.3.3. Forecasting

This subsection develops the in-sample forecasting exercise for the 2020 oil market disruption. We first describe the pattern-matching algorithm that underlies our prediction strategy, then present the complete forecast table with crash and survival probabilities for both components, and finally discuss the role of risk thresholds in generating predictions.

S.3.3.1. Algorithm

Our prediction strategy rests on the theoretical result of Proposition 3.3: during an extreme event, the trajectory of the aggregate process concentrates around a specific normalized pattern $\vartheta \boldsymbol{d}_{j_0,k}/\|\boldsymbol{d}_{j_0,k}\|$. These pattern structures are defined by four essential elements: the shape derived from the coefficient sequence $\boldsymbol{d}_{j,k}$; the component index $j \in \{1, \ldots, J\}$ identifying which latent process is driving the event; the time shift $k_0 \in \mathbb{Z}$ indicating the position within the pattern; and the sign $\vartheta \in \{-1, +1\}$ reflecting upward or downward movements.

The algorithm proceeds in four steps:

1. **Observation.** Observe the initial $m+1$ observations of the emerging extreme event ($m = 20$ throughout).
2. **Pattern matching.** Match the observed trajectory to the collection of theoretical patterns derived from the estimated $\mathcal{G}\alpha\mathcal{S}$ model, thereby identifying the component index j_0, the time shift k_0, and the sign ϑ_0.
3. **Probability computation.** For each future horizon $h \geq 1$, compute:

$$\mathbb{P}(\text{crash at } h) = |\psi_{j_0}|^{\alpha k}(1 - |\psi_{j_0}|^{\alpha}),$$
$$\mathbb{P}(\text{survive beyond } h) = |\psi_{j_0}|^{\alpha h}.$$

4. **Forecast generation.** Given a risk threshold $p \in \{0.90, 0.95, 0.99\}$, forecast the trajectory $\hat{\psi}_{j_0}^{-(h-k_0)} \cdot X_{t_0}$ until $1 - |\psi_{j_0}|^{\alpha h} > p$, at which point the crash is predicted.

For the 2020 episode, the cut-off date is January 2020. Pattern matching yields $k_0 = 3$ for Component 1 ($\hat{\psi}_1 = 0.7989$) and $k_0 = 1$ for Component 2 ($\hat{\psi}_2 = 0.8470$).

S.3.3.2. Prediction table

Table S.31 reports the predicted trajectory values, crash probabilities, and survival probabilities at each weekly horizon for both components, from the January 2020 cut-off through May 2020.

Table S.31: In-sample bubble forecast: predicted values and crash/survival probabilities (cut-off: January 2020, risk threshold: 99%)

		Component 1 ($k_0 = 3$, $\hat{\psi}_1 = 0.7989$)			Component 2 ($k_0 = 1$, $\hat{\psi}_2 = 0.8470$)		
Date	h	Forecast	Crash at h	Survive at h	Forecast	Crash at h	Survive at h
2020-01-05	0	11.2714	–	–	11.2714	–	–
2020-01-12	1	14.1087	–	–	13.3068	0.2164	0.7836
2020-01-19	2	17.6601	–	–	15.7098	0.3859	0.6141
2020-01-26	3	22.1056	0.6281	0.3719	18.5467	0.5188	0.4812
2020-02-02	4	27.6701	0.7326	0.2674	21.8958	0.6229	0.3771
2020-02-09	5	34.6325	0.8077	0.1923	25.8498	0.7045	0.2955
2020-02-16	6	43.3537	0.8617	0.1383	30.5178	0.7684	0.2316
2020-02-23	7	54.2668	0.9006	0.0994	36.0288	0.8185	0.1815
2020-03-01	8	67.9270	0.9285	0.0715	42.5349	0.8578	0.1422
2020-03-08	9	85.0258	0.9486	0.0514	50.2159	0.8886	0.1114
2020-03-15	10	106.4287	0.9630	0.0370	59.2839	0.9127	0.0873
2020-03-22	11	133.2193	0.9734	0.0266	69.9890	0.9316	0.0684
2020-03-29	12	166.7534	0.9810	0.0190	82.6283	0.9464	0.0536
2020-04-05	13	208.7292	0.9865	0.0135	97.5494	0.9580	0.0420
2020-04-12	14	0.0000*	0.9901	0.0099	115.1651	0.9671	0.0329
2020-04-19	15	0.0000*	0.9929	0.0071	135.9617	0.9742	0.0258
2020-04-26	16	0.0000*	0.9949	0.0051	160.5139	0.9798	0.0202
2020-05-03	17	0.0000*	0.9963	0.0037	189.4997	0.9842	0.0158
2020-05-10	18	0.0000*	0.9974	0.0026	223.7200	0.9876	0.0124
2020-05-17	19	0.0000*	0.9981	0.0019	0.0000*	0.9903	0.0097

Notes: Crash at h denotes $|\psi_{j_0}|^{\alpha k}(1 - |\psi_{j_0}|^{\alpha})$; Survive at h denotes $|\psi_{j_0}|^{\alpha h}$. *Crash predicted before this horizon at the 99% threshold (Component 1: $h = 14$; Component 2: $h = 19$). Forecast values after the predicted crash are set to zero. Pattern matching window: $m = 20$.

For Component 1 ($k_0 = 3$), crash probabilities become relevant only at $h = 3$; the bubble trajectory escalates from 11.27 to 208.73 over 13 periods before the 99% crash threshold is crossed at $h = 14$. For Component 2 ($k_0 = 1$), crash probabilities are immediately non-negligible (0.22 at $h = 1$), yet the lower growth rate sustains the trajectory through 18 periods, reaching 223.7 before the 99% threshold is crossed at $h = 19$.

S.3.3.3. Risk thresholds

The risk threshold parameter allows practitioners to customize predictions according to their risk tolerance. When the cumulative crash probability $1 - |\psi_{j_0}|^{\alpha k}$ exceeds the threshold, the model predicts a crash; otherwise, it anticipates continued growth. Higher thresholds generate more extreme bubble projections

before predicting a crash, while lower thresholds produce more conservative forecasts with earlier predicted crash points.

For Component 1, the predicted crash horizon shifts from $h = 7$ at the 90% threshold to $h = 14$ at the 99% threshold. For Component 2, the shift is from $h = 11$ to $h = 19$. In both cases, the 99% forecast trajectory most closely tracks the realized 2020 OVX path.

S.3.4. Per-component graphical diagnostics

This subsection collects the per-component crash probability profiles and forecast trajectories across the three risk thresholds (90%, 95%, 99%). Figures S.26 and S.27 display, for each component separately, the complete diagnostic output. Each figure is organized in three rows: the top row shows the crash/survival/cumulative probability curves as a function of horizon h; the middle row shows zoomed forecast trajectories; the bottom row situates the forecast within the full 2015–2025 sample.

The first component ($\hat{\psi}_1 = 0.7989$), with its slightly lower persistence, captures more abrupt movements: its contribution to the 2020 crisis is sharp but relatively brief, and the 99% threshold trajectory escalates from 11.27 to 208.73 before the predicted crash. The second component ($\hat{\psi}_2 = 0.8470$), with its higher persistence and dominant weight, tracks the more sustained explosive patterns: its trajectory reaches higher absolute values (up to 223.7) before the predicted collapse, reflecting the longer-lived nature of the underlying market anxiety.

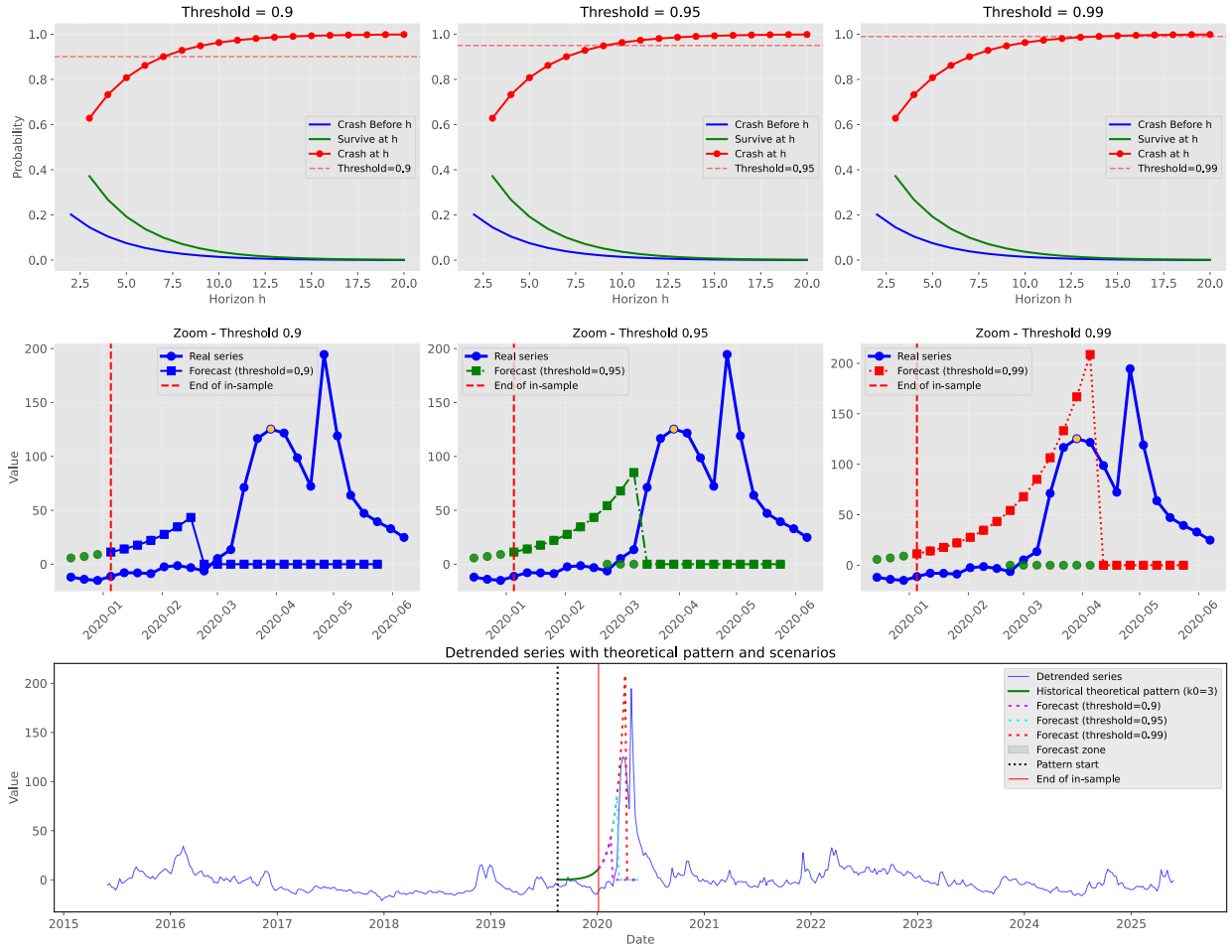

Figure S.26: In-sample forecast for the 2020 OVX bubble: Component 1 ($\hat{\psi}_1 = 0.7989$, $k_0 = 3$). *Top row:* crash probability profiles for risk thresholds 0.90 (left), 0.95 (center), and 0.99 (right). Each panel shows the probability of crashing at a given date (red line with circles), surviving beyond that date (green line), the cumulative crash probability (blue line), and the threshold (horizontal dashed red line). *Middle row:* zoomed-in forecast trajectories for each threshold; colored squares are predicted values; vertical dashed red line marks the cut-off (January 2020). *Bottom row:* full-sample view with the matched historical theoretical pattern ($k_0 = 3$) in green; forecasts at 0.90 (yellow), 0.95 (green dashed), and 0.99 (red dashed) thresholds; shaded area is the forecast zone. Pattern matching window: $m = 20$.

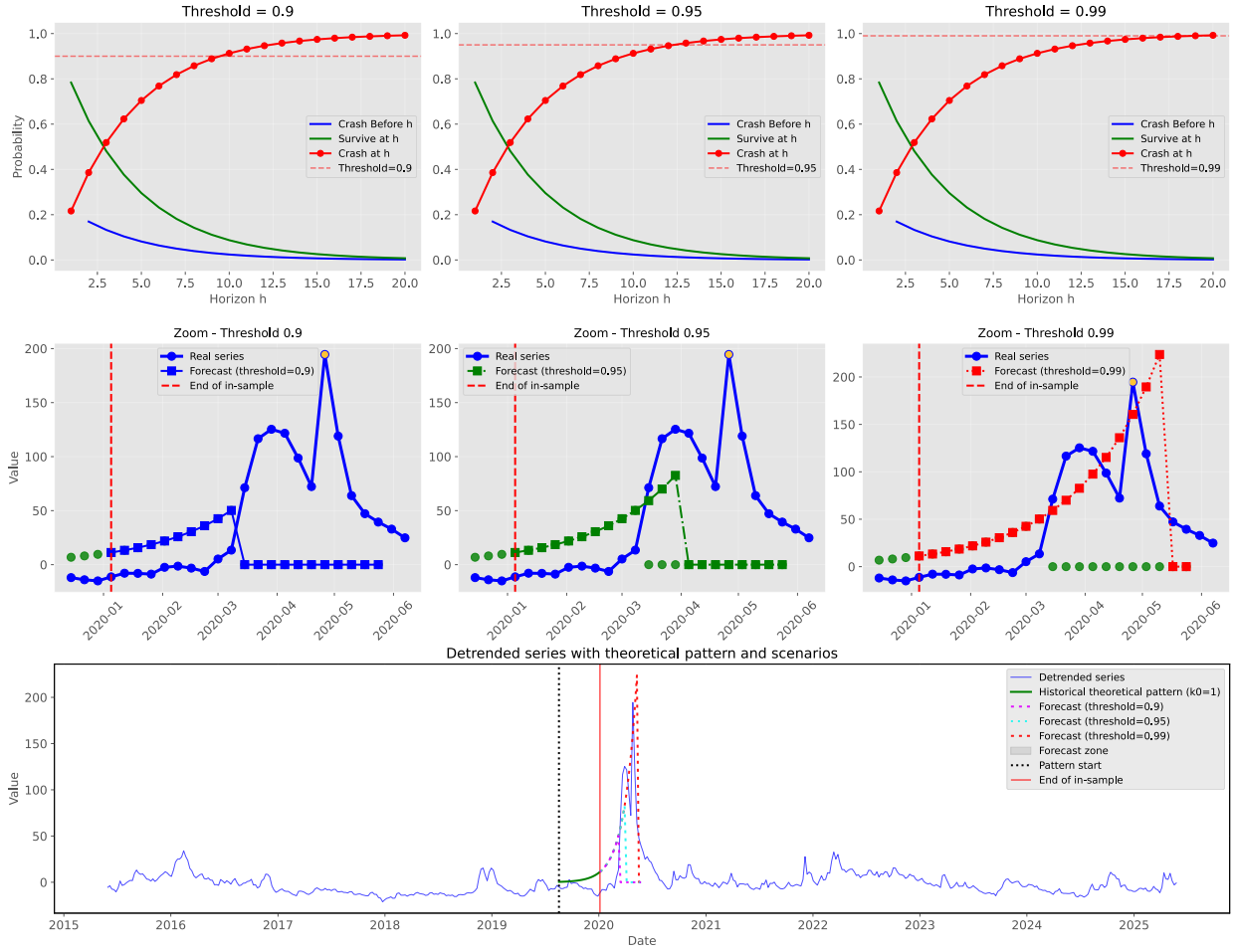

Figure S.27: In-sample forecast for the 2020 OVX bubble: Component 2 ($\hat{\psi}_2 = 0.8470$, $k_0 = 1$). Layout identical to Figure S.26. The historical theoretical pattern ($k_0 = 1$) is shown in green in the bottom row. Compared to Component 1, crash probabilities build more gradually but the forecasted trajectory reaches higher absolute values before the predicted crash, reflecting the higher persistence and dominant weight ($\hat{\pi}_2 = 0.72$) of this component. Pattern matching window: $m = 20$.

References

Politis, D.N., and J.P., Romano. 1994. Large Sample Confidence Regions Based on Subsamples under Minimal Assumptions. *The Annals of Statistics*, 22(4), 2031–2050.

Politis, D.N., Romano, J.P., and M., Wolf. 1999. *Subsampling*. Springer.

de Truchis, G., Thomas, A., L. Vaudrée (2025). Deconvolution and Filtering of Non-Causal Alpha-Stable Processes. *On going paper*.